arXiv:2206.11409v1 [astro-ph.EP] 22 Jun 2022

Systematic KMTNet Planetary Anomaly Search. VI. Complete Sample of 2018 Sub-Prime-Field Planets

Youn Kil Jung[1,2], Weicheng Zang[3], Cheongho Han[4], Andrew Gould[5,6], Andrzej Udalski[7],
(Lead Authors)
Michael D. Albrow[8], Sun-Ju Chung[1], Kyu-Ha Hwang[1], Yoon-Hyun Ryu[1], In-Gu Shin[4],
Yossi Shvartzvald[9], Hongjing Yang[3], Jennifer C. Yee[10], Sang-Mok Cha[1,11], Dong-Jin Kim[1],
Seung-Lee Kim[1], Chung-Uk Lee[1], Dong-Joo Lee[1], Yongseok Lee[1,11], Byeong-Gon Park[1,2],
Richard W. Pogge[6]
(The KMTNet Collaboration)
Przemek Mróz[7], Michał K. Szymański[7], Jan Skowron[7], Radek Poleski[7], Igor Soszyński[7],
Paweł Pietrukowicz[7], Szymon Kozłowski[7], Krzysztof Ulaczyk[12], Krzysztof A. Rybicki[7,9],
Patryk Iwanek[7], Marcin Wrona[7]
(The OGLE Collaboration)

[1]*Korea Astronomy and Space Science Institute, Daejon 34055, Republic of Korea*

[2]*Korea University of Science and Technology, Korea, (UST), 217 Gajeong-ro, Yuseong-gu, Daejeon, 34113, Republic of Korea*

[3] *Department of Astronomy, Tsinghua University, Beijing 100084, China*

[4]*Department of Physics, Chungbuk National University, Cheongju 28644, Republic of Korea*

[5]*Max-Planck-Institute for Astronomy, Königstuhl 17, 69117 Heidelberg, Germany*

[6]*Department of Astronomy, Ohio State University, 140 W. 18th Ave., Columbus, OH 43210, USA*

[7]*Astronomical Observatory, University of Warsaw, Al. Ujazdowskie 4, 00-478 Warszawa, Poland*

[8]*University of Canterbury, Department of Physics and Astronomy, Private Bag 4800, Christchurch 8020, New Zealand*

[9]*Department of Particle Physics and Astrophysics, Weizmann Institute of Science, Rehovot 76100, Israel*

[10] *Center for Astrophysics | Harvard & Smithsonian, 60 Garden St., Cambridge, MA 02138, USA*

[11]*School of Space Research, Kyung Hee University, Yongin, Kyeonggi 17104, Republic of Korea*

[12]*Department of Physics, University of Warwick, Gibbet Hill Road, Coventry, CV4 7AL, UK*

ABSTRACT

We complete the analysis of all 2018 sub-prime-field microlensing planets identified by the KMTNet AnomalyFinder. Among the 9 previously unpublished events with clear planetary solutions, 6 are clearly planetary (KMT-2018-BLG-0030, KMT-2018-BLG-0087, KMT-2018-BLG-0247, OGLE-2018-BLG-0298, KMT-2018-BLG-2602, and OGLE-2018-BLG-1119), while the remaining 3 are ambiguous in nature. In addition, there are 8 previously published sub-prime field planets that were selected by the AnomalyFinder algorithm. Together with a companion paper (Gould et al. 2022) on 2018 prime-field planets, this work lays the basis for the first statistical analysis of the planet mass-ratio function based on planets identified in KMTNet data. As expected (Zhu et al. 2014), half (17/33) of the 2018 planets likely to enter the mass-ratio analysis have non-caustic-crossing anomalies. However, only 1 of the 5 non-caustic anomalies with planet-host mass ratio $q < 10^{-3}$ was discovered by eye (compared to 7 of the 12 with $q > 10^{-3}$), showing the importance of the semi-automated AnomalyFinder search.

Subject headings: gravitational lensing: micro

1. Introduction

This paper completes the publication of all planetary events that were identified by the KMTNet AnomalyFinder algorithm (Zang et al. 2021b, 2022) that occurred during the 2018 season within the 21 sub-prime KMTNet fields. It is a companion to a paper on the 2018 prime-field planets by Gould et al. (2022), which analyzed 10 new planetary (or potentially planetary) events, and summarized 4 previous AnomalyFinder 2018 prime-field discoveries (Wang et al. 2022; Hwang et al. 2022), as well as 12 previously analyzed planetary (or possibly planetary) events that were recovered by AnomalyFinder. These 26 events are listed in their Table 11. The above references are, respectively, Papers I, IV, II, III, and V, in the AnomalyFinder series. The locations and cadences of the KMTNet fields are shown in Figure 12 of Kim et al. (2018a). The prime fields are those with nominal cadences of $\Gamma = 2\,\mathrm{hr}^{-1}$, namely, BLG01, BLG02, BLG03, BLG41, BLG42, and BLG43. We label

the (7, 10, 3) remaining fields, with respective nominal cadences $\Gamma = (1.0, 0.4, 0.2)\,\mathrm{hr}^{-1}$, as "sub-prime".

The AnomalyFinder (Zang et al. 2022) identified a total of 173 anomalous events (from an underlying sample of 1728 sub-prime-field events), which it classified as "planet" (17), "planet/binary" (4), "binary/planet" (19), "binary" (126), and "finite source" (7). Among the 126 in the "binary" classification, 35 were judged by eye to be unambiguously non-planetary in nature. Among the 17 in the "planet" classification, 7 were either previously published (5) or in preparation (2). Among the 4 in the "planet/binary" classification, one was in preparation, and among the 19 in the "binary/planet" classification one was a previously published planet. None of the events that were classified as "binary" or "finite source" were previously published (or in preparation) planets.

The results from Gould et al. (2022) and this paper can be combined with a detection efficiency analysis (Zang, Jung et al., in preparation) to derive the first mass-ratio function based on the KMTNet project. We refer the reader to the introduction of Gould et al. (2022) for the general framework of this approach.

2. Observations

The description of the observations is nearly identical to that in Gould et al. (2022) except that the events analyzed here are derived from 1728 sub-prime events that were subjected to the AnomalyFinder algorithm compared to 843 prime-field events in Gould et al. (2022). In particular, the KMTNet data are taken from three identical 1.6m telescopes, each equipped with cameras of 4 deg^2 (Kim et al. 2016) and located in Australia (KMTA), Chile (KMTC), and South Africa (KMTS). When available, our general policy is to include Optical Gravitational Lensing Experiment (OGLE) and Microlensing Observations in Astrophysics (MOA) data in the analysis. However, none of the 9 events analyzed here were alerted by MOA. OGLE data were taken using their 1.3m telescope with 1.4 deg^2 field of view at Las Campanas Observatory in Chile. For the light-curve analysis, we use only the I-band data.

As in Gould et al. (2022), Table 1 gives basic observational information about each event. Column 1 gives the event names in the order of discovery (if discovered by multiple teams), which enables cross identification. The nominal cadences are given in column 2, and column 3 shows the first discovery date. The remaining four columns show the event coordinates in the equatorial and galactic systems. Events with OGLE names were originally discovered by the OGLE Early Warning System (Udalski et al. 1994; Udalski 2003). KMT-named events with alert dates were originally discovered by the KMT AlertFinder system

(Kim et al. 2018b), while the others were discovered post-season by the EventFinder system (Kim et al. 2018a).

To the best of our knowledge, there were no ground-based follow-up observations of any of these events. KMT-2018-BLG-0173 was observed by *Spitzer* as part of a large-scale microlensing program (Yee et al. 2015), but these data do not show a discernible signal.

The KMT and OGLE data were reduced using difference image analysis (Tomaney & Crotts 1996; Alard & Lupton 1998), as implemented by each group, i.e., Albrow et al. (2009) and Woźniak (2000), respectively.

3. Light Curve Analysis

3.1. Preamble

We present here a compressed version of Section 3.1 of Gould et al. (2022) of the common features of the light-curve analysis. The reader who is interested in more details should consult that work.

All of the events can be initially approximated by 1L1S models, which are specified by three Paczyński (1986) parameters, $(t_0, u_0, t_{\rm E})$, i.e., the time of lens-source closest approach, the impact parameter in units of $\theta_{\rm E}$ and the Einstein timescale,

$$t_{\rm E} = \frac{\theta_{\rm E}}{\mu_{\rm rel}}; \qquad \theta_{\rm E} = \sqrt{\kappa M \pi_{\rm rel}}; \qquad \kappa \equiv \frac{4\,G}{c^2\,{\rm au}} \simeq 8.14\,\frac{\rm mas}{M_\odot}, \tag{1}$$

where M is the lens mass, $\pi_{\rm rel}$ and $\boldsymbol{\mu}_{\rm rel}$ are the lens-source relative parallax and proper-motion, respectively, and $\mu_{\rm rel} \equiv |\boldsymbol{\mu}_{\rm rel}|$. The notation "$nLm$S" means n lenses and m sources. In addition, to these 3 non-linear parameters, there are 2 flux parameters, (f_S, f_B), that are required for each observatory, representing the source flux and the blended flux.

We then search for "static" 2L1S solutions, which generally require 4 additional parameters (s, q, α, ρ), i.e., the planet-host separation in units of $\theta_{\rm E}$, the planet-host mass ratio, the angle of the source trajectory relative to the binary axis, and the angular source size normalized to $\theta_{\rm E}$, i.e., $\rho = \theta_*/\theta_{\rm E}$.

We first conduct a grid search with (s, q) held fixed at a grid of values and the remaining 5 parameters allowed to vary in a Monte Carlo Markov chain (MCMC). After we identify one or more local minima, we refine these by allowing all 7 parameters to vary.

We often make use of the heuristic analysis introduced by Hwang et al. (2022) and modified by Ryu et al. (2022) based on further investigation in Gould et al. (2022). If a

brief anomaly at $t_{\rm anom}$ is treated as due to the source crossing the planet-host axis, then one can estimate two relevant parameters

$$s^\dagger_\pm = \frac{\sqrt{4+u^2_{\rm anom}} \pm u_{\rm anom}}{2}; \quad \tan\alpha = \frac{u_0}{\tau_{\rm anom}}, \tag{2}$$

where $u^2_{\rm anom} = \tau^2_{\rm anom} + u^2_0$ and $\tau_{\rm anom} = (t_{\rm anom} - t_0)/t_{\rm E}$. Usually, $s^\dagger_+ > 1$ corresponds to anomalous bumps and $s^\dagger_- < 1$ corresponds to anomalous dips. This formalism predicts that if there are two degenerate solutions, $s_\pm$, then they both have the same α and that there exists a $\Delta \ln s$ such that

$$s_\pm = s^\dagger_{\rm pred} \exp(\pm \Delta \ln s), \tag{3}$$

where α and $s^\dagger$ are given by Equation (2). To test this prediction in individual cases, we can compare the purely empirical quantity $s^\dagger \equiv \sqrt{s_+ s_-}$ with prediction from Equation (2), which we always label with a subscript, i.e., either $s^\dagger_+$ or $s^\dagger_-$. This formalism can also be used to find "missing solutions" that have been missed in the grid search, as was done, e.g., for the case of KMT-2021-BLG-1391 (Ryu et al. 2022).

For cases in which the anomaly is a dip, the mass ratio q can be estimated,

$$q = \Big(\frac{\Delta t_{\rm dip}}{4\, t_{\rm E}}\Big)^2 \frac{s^\dagger}{|u_0|} |\sin^3\alpha|, \tag{4}$$

where $\Delta t_{\rm dip}$ is the full duration of the dip. In some cases, we investigate whether the microlens parallax vector,

$$\boldsymbol{\pi}_{\rm E} \equiv \frac{\pi_{\rm rel}}{\theta_{\rm E}} \frac{\boldsymbol{\mu}_{\rm rel}}{\mu_{\rm rel}} \tag{5}$$

can be constrained by the data. When both $\pi_{\rm E}$ and $\theta_{\rm E}$ are measured, they can be combined to yield,

$$M = \frac{\theta_{\rm E}}{\kappa \pi_{\rm E}}; \qquad D_L = \frac{\rm au}{\theta_{\rm E}\pi_{\rm E} + \pi_S}, \tag{6}$$

where D_L is the distance to the lens and π_S is the parallax of the source.

To model the parallax effects due to Earth's orbital motion, we add two parameters $(\pi_{{\rm E},N}, \pi_{{\rm E},E})$, which are the components of $\boldsymbol{\pi}_{\rm E}$ in equatorial coordinates. We also add (at least initially) two parameters $\boldsymbol{\gamma} = [(ds/dt)/s, d\alpha/dt]$, where $s\boldsymbol{\gamma}$ are the first derivatives of projected lens orbital position at t_0, i.e., parallel and perpendicular to the projected separation of the planet at that time, respectively. In order to eliminate unphysical solutions, we impose a constraint on the ratio of the transverse kinetic to potential energy,

$$\beta \equiv \Big|\frac{\rm KE}{\rm PE}\Big| = \frac{\kappa M_\odot {\rm yr}^2}{8\pi^2} \frac{\pi_{\rm E}}{\theta_{\rm E}} \gamma^2 \Big(\frac{s}{\pi_{\rm E} + \pi_S/\theta_{\rm E}}\Big)^3 < 0.8. \tag{7}$$

It often happens that $\boldsymbol{\gamma}$ is neither significantly constrained nor significantly correlated with $\boldsymbol{\pi}_{\rm E}$. In these cases, we suppress these two degrees of freedom.

Particularly if there are no sharp caustic-crossing features in the light curve, 2L1S events can be mimicked by 1L2S events. Where relevant, we test for such solutions by adding at least 3 parameters $(t_{0,2}, u_{0,2}, q_F)$ to the 1L1S models. These are the time of closest approach and impact parameter of the second source and the ratio of the second to the first source flux in the I-band. If either lens-source approach can be interpreted as exhibiting finite source effects, then we must add one or two further parameters, i.e., ρ_1 and/or ρ_2. And, if the two sources are projected closely enough on the sky, one must also consider source orbital motion.

In a few cases, we make kinematic arguments that solutions are unlikely because their inferred proper motions $\mu_{\rm rel}$ are too small. These arguments rely on the fact that the fraction of events with proper motions less than a given $\mu_{\rm rel} \ll \sigma_\mu$ is

$$p(\leq \mu_{\rm rel}) = \frac{(\mu_{\rm rel}/\sigma_\mu)^3}{6\sqrt{\pi}} \rightarrow 4 \times 10^{-3} \Big(\frac{\mu_{\rm rel}}{1\,{\rm mas\,yr^{-1}}} \Big)^3, \tag{8}$$

where (following Gould et al. 2021) we approximate the bulge proper motions as an isotropic Gaussian with dispersion $\sigma_\mu = 2.9\,{\rm mas\,yr^{-1}}$. For example, $p(\leq 0.5\,{\rm mas\,yr^{-1}}) = 5 \times 10^{-4}$ and $p(\leq 0.1\,{\rm mas\,yr^{-1}}) = 4 \times 10^{-6}$.

3.2. KMT-2018-BLG-0030

Figure 1 shows a low-amplitude ($\Delta I \simeq 0.4$) microlensing event, peaking at $t_0 = 8271.46$ and punctuated by a short bump at $t_{\rm anom} \simeq 8248.0$, i.e., -23.46 days before peak. Assuming that the source is unblended (as is reasonable, see below), the remaining Paczyński (1986) parameters are $u_0 = 0.90$ and $t_{\rm E} = 28\,{\rm days}$. Then $\tau_{\rm anom} = -0.84$ and $u_{\rm anom} = 1.23$. Hence, Equation (2) predicts $s_+^\dagger = 1.79$ and $\alpha = 133^\circ$.

We initially (as usual) conduct the grid search with free blending. This yields a result that is consistent with zero blending, but with a relatively large error, $f_B/f_S \simeq -0.14 \pm 0.14$. The extinction from the KMT website (ultimately derived from Gonzalez et al. 2012, using $A_I = 7\,A_K$), $A_I = 3.25$, implies a dereddened baseline magnitude that is brighter than the clump. The distribution of blending fractions for microlensing events associated with such very bright stars is generally bimodal, i.e., either very low because the apparent bright star is the source, or very high because a random field star is the source. Hence, all evidence is consistent with very low blending and we impose zero blending. The grid search returns only a single solution, whose refinement is shown in Table 2. The resulting $\alpha = 134.8^\circ$ is

in reasonable accord the heuristic prediction, while the value of $s = s_{\rm outer} = 1.58$, would seem to suggest a second solution at $s_{\rm inner} = (s_+^\dagger)^2/s_{\rm outer} = 2.03$. That is, Figure 1 shows the source passing "outside" the planetary caustic, so that the "inner/outer degeneracy" (Gaudi & Gould 1997) would seem to suggest a second solution with the source passing inside the planetary caustic. We specifically search for such a solution, in case that it was somehow missed by the grid search, by seeding the alternate parameters suggested by the heuristic analysis. We locate an "inner" solution, but it is disfavored by $\Delta\chi^2 = 208$, thus confirming its rejection at the grid-search stage.

As shown in Figure 1, the bump is featureless, so that it could in principle be generated by a second source rather than a second lens (Gaudi 1998). We therefore investigate 1L2S solutions but find that these are excluded by $\Delta\chi^2 = 100.5$.

Such featureless bumps can also, in principle, be caused by a large source passing over one of the two caustics due to a minor-image perturbation (i.e., $s < 1$). As mentioned above, the grid search did not return any such solution. Nevertheless, as a matter of due diligence, we specifically search for these. However, the best one has extreme negative blending $(f_B/(f_B + f_S)) = -5.5$, and $\Delta\chi^2 = 34$. When we enforce zero blending, the resulting models do not even approximate the observed light curves. Thus, $s < 1$ solutions are ruled out.

Table 2 indicates that this is a super-Jovian mass-ratio planet, $\log q = -2.56$.

Due to the low amplitude of the event (and so, relatively poorly constrained blending in a free fit), we do not attempt to measure the microlens parallax, $\boldsymbol{\pi}_{\rm E}$. Finally, we note that $\rho < 0.112$ (at $2.5\,\sigma$) is only weakly constrained. We will give quantitative expression to this weakness in Sections 4.1 and 5.1.

KMT-2018-BLG-0030 is one of three previously known planets that are analyzed here for the first time.

3.3. KMT-2018-BLG-0087

Figure 2 shows an approximately 1L1S light curve with Paczyński (1986) parameters $t_0 = 8281.73$, $u_0 = 0.53$, and $t_{\rm E} = 4.55\,$days, punctuated by a short dip at $t_{\rm anom} = 8281.1$, i.e., $\tau_{\rm anom} = -0.138$. The dip is featureless, while $u_0 \gg |\tau_{\rm anom}|$, indicating a roughly vertical source trajectory. Hence, we expect two solutions (inner/outer degeneracy) with $\alpha = 285^\circ$ and $s_-^\dagger = 0.767$. The full duration of the dip is $\Delta t_{\rm dip} = 1.0\,$days. Equation (4) then predicts $q = 3.9 \times 10^{-3}$.

The grid search indeed returns two solutions, whose refinement leads to the parameters given in Table 3. These precisely confirm the first two heuristic predictions, with $\alpha = 286°$ and $s^\dagger \equiv \sqrt{s_{\rm inner} s_{\rm outer}} = 0.757$, while (as is often the case, Hwang et al. 2022), the mass-ratio prediction is only qualitatively confirmed. The outer solution is significantly (but not overwhelmingly) favored at $\Delta\chi^2 = 5.3$.

This is another super-Jovian mass-ratio planet, with $\log q \simeq -2.65$.

While the constraint on ρ, i.e., $\rho < 0.110$ or $\rho < 0.096$ (at $2.5\,\sigma$) is very similar to KMT-2018-BLG-0030 (and, as we will see in Section 4, the source sizes are also similar), this constraint will, in contrast to that case, ultimately prove to be significant. This is because the Einstein timescale is much shorter. Indeed, at $t_{\rm E} \sim 4.55\,$days, KMT-2018-BLG-0087 is one of the shortest bound-planet events yet detected (Ryu et al. 2021). As we will discuss in Sections 4.2 and 5.2, these characteristics imply that the host is most likely a low-mass star (or possibly brown dwarf) in the bulge.

Although the anomaly is well-fitted by a minor-image "dip" and therefore is not expected to be compatible with a 1L2S model, we nevertheless check this possibility as a matter of due diligence. As anticipated, we find that 1L2S is ruled out, with $\Delta\chi^2 = \chi^2(\text{1L2S}) - \chi^2(\text{2L1S}) = 100.1$.

Due to the extreme shortness of the event, we do not attempt to measure the microlens parallax, $\boldsymbol{\pi}_{\rm E}$.

Of minor note, KMT-2018-BLG-0087 lies in the very small region of overlap between KMT fields BLG14 and BLG15 and therefore is a rare case of a sub-prime-field event with a $\Gamma = 2\,{\rm hr}^{-1}$ cadence.

3.4. KMT-2018-BLG-0247

Figure 3 shows a short ($\sim 0.7\,$day) double horned profile centered at $t_{\rm anom} = 8305.70$ just after the peak of a normal 1L1S event with parameters $t_0 = 8308.42$, $u_0 = 0.065$, and $t_{\rm E} = 10.6\,$days, yielding $\tau_{\rm anom} = 0.0264$, $u_{\rm anom} = 0.070$ and so $s_+^\dagger = 1.036$ and $\alpha = 68°$.

The grid search returns two solutions, whose refinements are given in Table 4 and whose geometries are shown in Figure 3. Note that both geometries have the source crossing the neck of a resonant caustic, which does not appear to be directly related to either of the degeneracies (inner/outer of Gaudi & Gould 1997 or close/wide of Griest & Safizadeh 1998) that were predicted in advance and that were unified in Equation (2) by Ryu et al. (2022) following the conjecture of Yee et al. (2021). Subsequently, Zhang & Gaudi (2022)

investigated the origins of unification at the level of the lens equation. Nevertheless, the two solutions combine to yield $s^\dagger \equiv \sqrt{s_+ s_-} = 1.043$, in excellent agreement with the prediction.

Both solutions imply another super-Jovian mass-ratio planet, $\log q = -2.2$.

Figure 3 shows that only the caustic entrance is resolved. The fact that the source enters the caustic at different angles in the two solutions leads to different values of ρ, which are proportional to the cosine of this angle. Note that if the exit had been resolved by the data, then the degeneracy would have been broken. In this sense, it is accidental.

Due to the short $t_{\rm E}$, we do not attempt to measure the microlens parallax, $\boldsymbol{\pi}_{\rm E}$.

KMT-2018-BLG-0247 is one of three previously known planets that are analyzed here for the first time.

3.5. OGLE-2018-BLG-0298

Figure 4 shows a brief bump on the falling wing at $t_{\rm anom} = 8190.6$ of a normal 1L1S event with parameters $t_0 = 8188.74$, $u_0 = 0.021$, and $t_{\rm E} = 32\,{\rm days}$, yielding $\tau_{\rm anom} = 0.058$, $u_{\rm anom} = 0.062$, and so $s_+^\dagger = 1.031$ and $\alpha = 20^\circ$.

The grid search returns two solutions, whose refinements are shown in Table 5. Based on caustic geometries shown in Figure 4, these might plausibly be identified as a case of the "inner/outer" degeneracy, although this would be very far from the original conception of Gaudi & Gould (1997). Even so, the parameters $s^\dagger \equiv \sqrt{s_+ s_-} = 1.016$ and $\alpha = 20^\circ$ are in reasonably good agreement with the heuristic prediction. Note that the wide solution has a cusp approach at about 8192.5, which is also preceded by a dip. However, these putative features are not probed by any data. See Figure 4. In this sense, the degeneracy is accidental.

Because the bump is featureless, we check for 1L2S solutions, but we find that these are excluded at $\Delta\chi^2 = 33.7$. In addition, the solution gives $t_{*,2} = \rho_2 t_{\rm E} = 0.21\,{\rm days}$ and $q_F = 0.013$, indicating that the second source lies about 7 mag below the clump (see Section 4.4), and so implying $\theta_{*,2} \sim 0.3\,\mu{\rm as}$. These yield $\mu_{\rm rel} = \theta_{*,2}/t_{*,2} = 0.55\,{\rm mas\,yr^{-1}}$, which is quite improbable according to Equation (8). Therefore, we consider the 1L2S models to be decisively excluded.

Given the intermediate timescale, $t_{\rm E} \sim 32\,{\rm days}$, and moderately faint source, $I_S \sim 20$, it would be unlikely that a full, 2-dimensional (2-D) parallax could be measured. Nevertheless, a 1-D parallax measurement is plausible. For example, (Gould et al. 2022) found two such cases. See their Figure 3. Indeed, for the four cases, (close $u_0 > 0$, wide $u_0 > 0$, close $u_0 < 0$,

wide $u_0 < 0$) we find four, very similar, highly-elongated error ellipses, with $(\pi_{\rm E,\parallel}, \pi_{\rm E,\perp}, \psi) = (0.00 \pm 0.11, -0.08 \pm 0.63, 272.1^\circ)$, $(-0.02 \pm 0.11, -0.06 \pm 0.68, 272.0^\circ)$, $(0.00 \pm 0.11, -0.19 \pm 0.64, 271.2^\circ)$, and $(-0.02 \pm 0.11, -0.24 \pm 0.64, 271.5^\circ)$, respectively[1]. Here $\pi_{\rm E,\parallel}$, and $\pi_{\rm E,\perp}$ are the minor and major axes of the error ellipse, which are so named because their orientation angle ψ (north through east) is approximately parallel to the projected position of the Sun at the peak of the event. In all cases, the improvement from adding parallax (and orbital motion, see Section 3.1) is $\Delta\chi^2 < 1$ for four degrees of freedom. We find that in all four cases, the numerical contours are well described as Gaussian realizations of the 3-parameter representations listed above.

Nevertheless, the constraint implied by this parallax measurement is moderately significant. As discussed by Han et al. (2016), we are not trying to "detect" parallax: it is known a priori that $\pi_{\rm E} \equiv \pi_{\rm rel}/\theta_{\rm E}$ is strictly non-zero. Hence, limits, even 1-D limits, on the parallax vector can be constraining when combined with prior information from a Galactic model. We discuss the implementation of these constraints in Section 5.4. Here, we only remark that the remaining parameters change by much less than their error bars, and they would change even less if we were to apply Galactic-model priors to the parallax. Therefore, we report the static-model solutions in Table 5.

This is a sub-Saturn mass-ratio planet, $\log q = -3.7$, the only securely planetary event in this paper to lie in this range. By comparison, among 2018 prime-field unambiguously planetary events that were newly discovered by AnomalyFinder, there were 5 with $q < 2 \times 10^{-4}$, namely, OGLE-2018-BLG-0383 (Wang et al. 2022), OGLE-2018-BLG-0506, OGLE-2018-BLG-0516, and OGLE-2018-BLG-0977 (Hwang et al. 2022), and OGLE-2018-BLG-1126 (Gould et al. 2022).

3.6. KMT-2018-BLG-2602

Figure 5 shows an approximately 1L1S light curve with parameters $t_0 = 8270.3$, $u_0 = 0.51$, and $t_{\rm E} = 98\,{\rm days}$, punctuated by a short, smooth bump at $t_{\rm anom} = 8243.8$, yielding $\tau_{\rm anom} = -0.27$ and $u_{\rm anom} = 0.58$, which imply $s_+^\dagger = 1.33$ and $\alpha = 118^\circ$.

The grid search returns two solutions, whose refined parameters are shown in Table 6. These agree with the heuristic predictions. In particular $s^\dagger \equiv \sqrt{s_+ s_-} = 1.35$. The close solution is favored by $\Delta\chi^2 = 10.4$, and we therefore choose it for our adopted solution.

[1]See Figure 3 of Park et al. (2004) for sign conventions, keeping in mind that OGLE-2018-BLG-0298 peaked before opposition while MOA-2003-BLG-037 peaked after opposition.

However, the mass ratios of two solutions are nearly identical: this is Jovian mass-ratio planet: $\log q = -2.8$. Figure 5 shows that the two caustic topologies are related by an "inner/outer" degeneracy in which (as is often the case), the "outer" topology has a resonant caustic.

Because the bump is featureless, it could in principle be generated by a second source, rather than a second lens. However, we find that 1L2S solutions are excluded at $\Delta\chi^2 = 30.7$. Moreover, from Table 6, we see that the second-source self-crossing time is $t_{*,2} \sim 3.9\,\mathrm{days}$. while the large flux ratio would imply that the second source lies about 7.7 mag below the clump, indicating a second-source radius $\theta_{*,2} \sim 0.3\,\mu\mathrm{as}$. Combined, these would imply $\mu_{\rm rel} = \theta_{*,2}/t_{*,2} = 0.028\,\mathrm{mas\,yr^{-1}}$, which is extraordinarily unlikely. See Equation (8).

By contrast, in the 2L1S solutions, there are only upper limits on ρ, so no such issues arise.

In spite of the long duration of the event, we do not attempt a parallax analysis because the baseline cannot be properly constrained within the 2018 season, and we find small photometric offsets between seasons that would render multi-season analysis questionable.

KMT-2018-BLG-2602 is one of three previously known planets that are analyzed here for the first time.

3.7. OGLE-2018-BLG-1119

Figure 6 shows an approximately 1L1S light curve with parameters, $t_0 = 8316.0$, $u_0 = 0.43$, and $t_{\rm E} = 40\,\mathrm{days}$, punctuated by a small bump before the peak at $t_{\rm anom} = 8310.7$, i.e., with $\tau_{\rm anom} = -0.133$, and so $u_{\rm anom} = 0.45$. These values predict $s_+^\dagger = 1.25$ and $\alpha = 106^\circ$.

The grid search yields two solutions, whose refinements are shown in Table 7. They confirm $s^\dagger \equiv \sqrt{s_+ s_-} = 1.24$ and $\alpha = 107^\circ$. Figure 6 shows that this is an inner/outer degeneracy in which the outer solution has a resonant caustic.

Given the featureless character of the bump (which, in the 2L1S models is explained by a ridge crossing), we also fit the event with a 1L2S model. Table 7 shows that this is disfavored by $\Delta\chi^2 = 14.0$. In itself, this argues strongly against the 1L2S hypothesis, but does not completely exclude it.

We therefore also investigate the physical plausibility of the 1L2S solution. Table 7 shows that $t_{*,2} \equiv \rho_2 t_{\rm E} = 1.40 \pm 0.27\,\mathrm{days}$ and $q_F = 4.2 \times 10^{-3}$. We will see in Section 4.6 that the latter implies that the second source lies ~ 10 mag below the clump, and hence

it has $\theta_{*,2} \sim 0.15\,\mu$as, implying $\mu_{\rm rel} = \theta_{*,2}/t_{*,2} \sim 0.039\,{\rm mas\,yr^{-1}}$. This is extraordinarily improbable, i.e., $p = 2 \times 10^{-7}$, according to Equation (8). Hence, we consider the 1L2S solution to be excluded by the combination of $\Delta\chi^2$ and kinematic arguments.

This is another Jovian-class mass-ratio planet, $\log q = -2.75$.

Due to the event's low amplitude and faint source, we do not attempt a microlens parallax analysis.

3.8. KMT-2018-BLG-0173

Figure 7 shows an approximately 1L1S light curve with parameters of (assuming zero blending) $t_0 = 8348.7$, $u_0 = 0.79$, and $t_{\rm E} = 52\,$days, punctuated by a small bump far out on the leading wing at $t_{\rm anom} = 8256$, i.e., with $\tau_{\rm anom} = -1.78$ and so $u_{\rm anom} = 1.95$. At this separation, the planetary caustics are generally small and weak. Hence, it is more likely that the featureless bump is due to the source at least partially enveloping a planetary caustic (either major or minor image), rather than crossing the ridge associated with a major-image caustic. We therefore report both branches of $s^\dagger_\pm$, i.e., $s^\dagger_- = 0.42$ and $s^\dagger_+ = 2.37$, with corresponding values of $\alpha_- = 156^\circ$ and $\alpha_+ = 336^\circ$.

The grid search indeed returns two solutions, whose refinements are shown in Table 8, and which are roughly in accord with these predictions. Note that the heuristic formalism naively predicts a second wide solution at $s_{\rm wide,2} = (s^\dagger)^2/s_{\rm wide} = 2.43$. This would basically correspond to the source enveloping the caustic from its left side (as opposed to the right-side envelopment shown in Figure 7). However, the error in s from Table 8 already essentially covers this alternative solution at $1.5\,\sigma$, and we find that seeding an MCMC with this solution leads to a convergence at the reported solution. Hence, there is a relatively large continuous degeneracy in s, rather than a discrete degeneracy.

Both solutions have Jovian-class mass ratios, $\log q = -3.0$. See Table 8.

Two arguments favor the close solution. First, $\Delta\chi^2 = 11.2$, which is significant but not overwhelming evidence. Second, while the close solution is consistent with small ρ (in particular, $\rho = 0$ is disfavored by only $\Delta\chi^2 = 3.5$), the wide solution is well localized at $\rho_{\rm wide} \sim 0.125$, corresponding to $t_{*,\rm wide} \sim 6.5\,$days. We will show in Section 4.7 that for the wide solution $\theta_{*,\rm wide} \sim 6.0\,\mu$as, which would imply $\mu_{\rm rel,wide} = \theta_{*,\rm wide}/t_{*,\rm wide} \sim 0.34\,{\rm mas\,yr^{-1}}$. According to Equation (8), this has a probability $p \sim 1.5 \times 10^{-4}$. (Alternatively, if we force $\rho = 0$, the best-fit solution has an additional $\Delta\chi^2 = 18.0$, which would be formally disfavored by a similar factor, $p = \exp(-(18.0 - 3.5)/2) = 7 \times 10^{-4}$.) The combination of these two

arguments leads us to strongly favor the close over the wide solution.

However, because the anomaly is a featureless bump, we must also check the 1L2S model. See Table 8. This model is disfavored by three different arguments. First, it is disfavored by $\Delta\chi^2 = 10.8$, i.e., very similar to the difference between the close and wide models. If Gaussian statistics applied, this would correspond to $p = 4.5 \times 10^{-3}$, which would effectively settle the matter. However, this χ^2 difference derives from subtle differences in the models over several weeks (see Figure 7), and so could be impacted by equally subtle long-term systematics, which would be difficult to track down. Hence, we look for additional evidence.

The second argument is that the best-fit color of the second source is essentially identical to that of the first source, $\Delta(V-I) \equiv (V-I)_2 - (V-I)_1 \simeq 0$, whereas its magnitude is $-2.5\log(q_F) = 7.5$ mag fainter, and hence should be substantially redder, $\Delta(V-I) \sim 1$. See Section 4.7. That is, if the 2L1S model is correct, the amplitude of the "bump" should be essentially identical in V and I, while for the 1L2S model, it should be suppressed by a factor $10^{-0.4\Delta(V-I)} \sim 0.4$. There are 6 V-band points (2 from each observatory) over portions of the bump that deviate from the 1L1S model by at least of order the V-band error bars (~ 0.03 mag), which track the I-band points (not shown). Unfortunately, this is a weak test because of the paucity of V-band data and the relatively large error bars. We find that if we enforce $\Delta(V-I) = 1$, then χ^2 is only increased by $\Delta\chi^2 = 2.5$. Nevertheless, in contrast to the $\Delta\chi^2 = 10.8$ difference from the I-band fit, this determination is not subject to potential systematic errors from long-term trends in the light curve: it is a purely differential measurement from V and I measurements taken under essentially identical conditions, just 2 minutes apart.

Third, a kinematic argument (similar to the one given above against the 2L1S wide solution) further argues against the 1L2S solution. The flux ratio, $q_F \sim 10^{-3}$ would imply $\theta_{*,2} \sim 0.3\,\mu$as for the radius of the second source. See Section 4.7. On the other hand, $t_{*,2} \sim 2.0$ days, implying $\mu_{\rm rel} \sim \theta_{*,2}/t_{*,2} = 0.055\,{\rm mas\,yr^{-1}}$. According to Equation (8), this would have probability $p < 10^{-6}$.

Nevertheless, we note that there is a partial loophole to this argument. While the MCMC is well localized near $\rho_2 \sim 0.04$, solutions with $\rho_2 \sim 0$ are excluded at only (an additional) $\Delta\chi^2 = 6.5$. Thus, a strict comparison of the 2L1S (close) solution and the 1L2S ($\rho_2 = 0$) solution, in effect, favors the former by $\Delta\chi^2 \sim 10.8 + 6.5 - 3.5 = 14.8$. Moreover, if we combine this preference, which is subject to effects of long-term systematics, with the source-color argument above, which does not, we obtain $\Delta\chi^2 \sim 14.8 + 2.5 = 16.3$.

We defer weighing these various pieces of evidence until Section 4.7, where we will

bring to bear additional information of the source-star characteristics in these three different models.

3.9. KMT-2018-BLG-1497

Figure 8 shows an approximately 1L1S light curve with parameters, $t_0 = 8229.1$, $u_0 = 0.21$, and $t_{\rm E} = 31\,{\rm days}$, with a short, possibly structured bump at $t_{\rm anom} = 8233.9$, yielding $\tau_{\rm anom} = +0.155$ and $u_{\rm anom} = 0.26$, which imply $s_+^\dagger = 1.14$ and $\alpha = 59^\circ$.

The grid search returns 3 solutions, whose refinements are shown in Table 9. Two of these approximately correspond to the heuristic prediction, with $s^\dagger = \sqrt{s_+ s_-} = 1.17$ and $\alpha = 55^\circ$. Although the discrepancies are modest in absolute terms, they are significantly larger than is typically the case. Figure 6 shows that while this is an inner/outer degeneracy, the outer solution has a caustic crossing (which is favored by the early KMTA points), while the inner solution does not. Hence, we do not expect the heuristic formalism to work perfectly.

More importantly, there is a third solution, in which the bump is due to an off-axis cusp approach. See Figure 6. Table 9 shows that the 3 solutions cover a factor 80 range of mass ratios, q, while the full range of χ^2 is only $\Delta\chi^2 = 4.2$. Hence, even if this could be confidently accepted as a planetary event, the planet's characteristics would be extremely uncertain.

Moreover, we find that there is a 1L2S model with $\Delta\chi^2 = 2.1$. See Table 9. Because ρ_2 is not confidently measured for this solution, we cannot make kinematic arguments against it.

Therefore, first, we cannot be confident that this is a planetary event, and second, even if it is, we cannot determine the planet's mass ratio. Therefore, this event should not be cataloged as "planetary", and, in particular, it should not enter mass-ratio studies.

Due to the ambiguous nature of the event, we do not attempt a microlens parallax analysis.

3.10. KMT-2018-BLG-1714

Figure 9 shows an approximately 1L1S light curve with parameters $t_0 = 8318.17$, $u_0 = 0.16$, and $t_{\rm E} = 3.2\,{\rm days}$, with a short bump defined by just two points at $t_{\rm anom} = 8318.10$, yielding $\tau_{\rm anom} = -0.022$ and $u_{\rm anom} = 0.16$, which imply $s_+^\dagger = 1.08$ and $\alpha = 98^\circ$. The two

points were taken in $\sim 1.5''$ seeing, which is good for KMTA, and also very similar to the previous 4 points. Similarly, the background was low and steady. There is nothing unusual about these points, so we conclude that the increase in recorded flux is of astrophysical origin.

However, a grid search returns three solutions, rather than the usual one or two. Two of these solutions constitute an inner/outer pair, with similar $\alpha = 97^\circ$ and $s^\dagger \equiv \sqrt{s_+ s_-} = 1.09$ to those anticipated from the heuristic analysis (see Table 10). However, the third solution has a completely different topology, in which the bump is generated by an off-axis cusp of a resonant caustic. See Figure 9. The mass ratio of this solution is about 3.5 times larger than those of the other two. While this solution is disfavored by $\Delta\chi^2 = 7.5$, it cannot be definitively excluded on these grounds.

Moreover, such a poorly traced bump could be due to an extra source rather than an extra lens. We find a 1L2S solution with $\Delta\chi^2 = 0.9$. Because ρ_2 is poorly constrained in this solution, we cannot develop arguments against it based on physical considerations, as we could in several other cases. Therefore, we cannot be certain that the anomaly of this event is due to a planet, and we cannot uniquely determine the mass ratio even if it is assumed to be a planet.

Hence, we specifically counsel against cataloging this event as planetary, and, in particular, we advise against it being used in mass-ratio studies.

Due to the ambiguous nature of the event, we do not attempt a microlens parallax analysis.

4. Source Properties

If ρ can be measured from the light curve, then one can use standard techniques (Yoo et al. 2004) to determine the angular source radius, θ_* and so infer $\theta_{\rm E}$ and $\mu_{\rm rel}$:

$$\theta_{\rm E} = \frac{\theta_*}{\rho}; \qquad \mu_{\rm rel} = \frac{\theta_{\rm E}}{t_{\rm E}}. \tag{9}$$

However, in contrast to the majority of published by-eye discoveries (but similarly to most of new AnomalyFinder discoveries reported in Zang et al. 2021b, 2022; Hwang et al. 2022; Gould et al. 2022), most of the planetary events reported in this paper have only upper limits on ρ, and these limits are mostly not very constraining. As discussed by Gould et al. (2022), in these cases, θ_* determinations are not likely to be of much use, either now or in the future. Nevertheless, the source color and magnitude measurement that are required inputs for these

determinations may be of use in the interpretation of future high-resolution observations, either by space telescopes or adaptive optics (AO) on large ground-based telescopes. Hence, like Gould et al. (2022), we calculate θ_* in all cases.

Our general approach is to obtain pyDIA (Albrow 2017) reductions of KMT data at one (or possibly several) observatory/field combinations. These yield the microlensing light curve and field-star photometry on the same system. We then determine the source color by regression of the V-band light curve on the I-band light curve, and the source magnitudes in I by regression on the best-fit model. While Gould et al. (2022) were able to calibrate these CMDs using published field star photometry from OGLE-III (Szymański et al. 2011) or OGLE-II (Szymański 2005; Kubiak & Szymański 1997; Udalski et al. 2002), only 2 of the 9 sub-prime-field events in this paper are covered by these catalogs. Hence, for the remaining 7, we work directly in the KMTC pyDIA magnitude system. Because the θ_* measurements depend only on photometry relative to the clump, they are unaffected by calibration. In the current context, calibration is only needed to interpret limits on lens light. Where relevant, we carry out an alternative approach to calibration, as we explicitly describe.

We then follow the standard method of Yoo et al. (2004). We adopt the intrinsic color of the clump $(V-I)_{0,\rm cl} = 1.06$ from Bensby et al. (2013) and its intrinsic magnitude from Table 1 of Nataf et al. (2013). We obtain $[(V-I),I]_{\rm S,0} = [(V-I),I]_{\rm S} + [(V-I),I]_{\rm cl,0} - [(V-I),I]_{\rm cl}$. We convert from V/I to V/K using the VIK color-color relations of Bessell & Brett (1988) and then derive θ_* using the relations of Kervella et al. (2004a,b) for giant and dwarf sources, respectively. After propagating errors, we add 5% in quadrature to account for errors induced by the overall method. These calculations are shown in Table 11. Where there are multiple solutions, only the one with the lowest χ^2 is shown. However, the values of θ_* can be inferred for the other solutions by noting the corresponding values of I_S in the event-parameter tables and using $\theta_* \propto 10^{-I_S/5}$. In any case, these are usually the same within the quoted error bars.

Where relevant, we report the astrometric offset of the source from the baseline object.

Comments on individual events follow.

4.1. KMT-2018-BLG-0030

As noted in Section 3.2, the free-blending fit is consistent with zero blending at the $1\,\sigma$ level, and we therefore enforced zero blending in the fit. We also find that the source position lies < 15 mas from the baseline object (i.e., within the measurement precision), which implies that if there is any blended light, it is almost certainly associated with the event, i.e., from

the lens itself, a companion to the lens, or a companion to the source. However, as the source is brighter than the clump (see Figure 10), and the error in the free-blending fit is large, we cannot place useful limits on the lens flux.

The $2.5\,\sigma$ limit $\rho < 0.112$, implies $t_* = \rho t_{\rm E} < 3.1\,{\rm days}$. Combined with the measurement $\theta_* = 8.5\,\mu{\rm as}$ from Table 11, this implies $\mu_{\rm rel} = \theta_*/t_* > 1.00\,{\rm mas\,yr^{-1}}$. According to Equation (8), this excludes $\sim 0.4\%$ of Galactic events. Hence, while we will include the ρ constraint (or, rather the corresponding constraint $\theta_{\rm E} > 76\,\mu{\rm as}$) in the Bayesian analysis of Section 5.1, the only real constraint will be from the measurement of $t_{\rm E}$.

We note that *Gaia* (Gaia Collaboration et al. 2016, 2018) reports a source proper motion of $\boldsymbol{\mu}_S(N,E) = (-7.79, -10.93) \pm (0.45, 0.67)\,{\rm mas\,yr^{-1}}$. If correct, the source would be moving at about $8.3\,{\rm mas\,yr^{-1}}$ relative to the bulge proper-motion centroid. Only of order 1.6% of bulge sources are moving this fast. However, the *Gaia* RUWE parameter is 2.2, indicating that the measurement may not be reliable. Hence, because the measurement is both unusual and possibly unreliable, we do not include it in the Bayesian analysis. In any case, because there is no significant constraint on $\mu_{\rm rel}$, the *Gaia* measurement would not have much effect even if it were included.

4.2. KMT-2018-BLG-0087

The source analysis is overall similar to the case of KMT-2018-BLG-0030 (see Section 4.1). The source position lies within $\sim 23\,{\rm mas}$ of the baseline object (consistent with measurement error), while the blended light is consistent with zero at $< 2\,\sigma$. Hence, if there is blended light, it would again be associated with the event. However, again, because the source is above the clump, while the blend could have at least 10% of the source light, no useful constraint can be put on lens light. Because the color and magnitude of the blend are not well-constrained (and because there is no clear evidence that the blend flux is different from zero), we do not display the blended light in Figure 10.

The upper limit $\rho < 0.110$ (or $\rho < 0.096$) is essentially the same as for KMT-2018-BLG-0030, but in this case, it leads to a much shorter limit, $t_* < 0.50\,{\rm days}$, and so to a proper-motion constraint, $\mu_{\rm rel} = \theta_*/t_* > 7.0\,{\rm mas\,yr^{-1}}$. This is significant and thus can play an important role in the Bayesian analysis in Section 5.2. In fact, we will use the full χ^2 versus ρ envelope, rather than a simple upper limit. Unfortunately, while *Gaia* has an entry for the source star, it does not report a parallax and proper-motion solution. However, this means that future iterations of the *Gaia* catalog may report a proper-motion measurement.

4.3. KMT-2018-BLG-0247

The source color measurement using KMTC led to a relatively blue color $(V-I)_{0,S} = 0.51 \pm 0.07$. Hence, we checked the result using KMTS data, but found a consistent result with a substantially larger error, $(V-I)_{0,S} = 0.57 \pm 0.16$. The results reported in Table 11 and shown in Figure 10 are the weighted average of the two measurements. Because of the dearth of such blue stars in the bulge (even at its location on the turnoff), it is likely that the true color is 1–1.5 σ redder. Nevertheless, we consider that our usual error treatment adequately allows for such variations.

As noted in Section 3.4, the two solutions have substantially different ρ measurements due to the different source angles relative to the caustic entrance. These lead to Einstein-radius and proper-motion measurements,

$$\theta_{\rm E} = 0.335 \pm 0.045\,{\rm mas}; \qquad \mu_{\rm rel} = 11.6 \pm 1.6\,{\rm mas\,yr^{-1}} \qquad ({\rm close}), \tag{10}$$

and

$$\theta_{\rm E} = 0.256 \pm 0.034\,{\rm mas}; \qquad \mu_{\rm rel} = 8.8 \pm 1.2\,{\rm mas\,yr^{-1}} \qquad ({\rm wide}). \tag{11}$$

Figure 10 shows that the blend is about 0.6 brighter and 0.2 mag bluer than the source. We find that the baseline object is separated by about 180 mas from the source, implying that the blend is about 300 mas from the source. We can robustly say that the lens is fainter than this blend, $I_{L,{\rm pyDIA}} > I_B = 20.46$ because a lens that was even within a few tenths of a mag of I_B would "force" the additional star that is responsible for the astrometric offset to be sufficiently separated to be resolved. However, this limit has almost no impact on bulge lenses because the field extinction, $A_I = 2.99$, implies that this limit only excludes bulge stars with $M_I \lesssim 2.8$, which are extremely rare. Moreover, disk lenses that are sufficiently massive to provide this light are already heavily disfavored by the relatively small $\theta_{\rm E}$ in Equations (10) and (11). Nevertheless, we include this limit in Section 5.3 for completeness.

4.4. OGLE-2018-BLG-0298

As for all other events in this paper, the OGLE-2018-BLG-0298 CMD is shown for $[(V-I), I]$. However, while the clump is clearly visible in Figure 10, the lower part of the clump merges into the background noise, which is due to high extinction. In principle, this could make it difficult to properly measure the mean I-band magnitude of the clump. On the other hand, the clump is approximately horizontal (which is the expected behavior provided that there is relatively little differential extinction across the field), implying that

the mean $(V-I)$ color of the clump is independent of height and so not significantly affected by growing noise at faint magnitudes.

We therefore measure the height, $I_{\rm cl}$, (but not the color) of the clump from an $[(I-K), I]$ diagram, which we construct by matching the KMTC pyDIA I-band measurements to the K-band measurements from the VVV catalog (Minniti et al. 2010, 2017). This measurement is illustrated in the "undersized panel" of Figure 11. We emphasize that the only purpose of this panel is to measure $I_{\rm cl}$, which is then reproduced in Figure 10 and in Table 11.

As shown in Figure 10, the source is blended with a clump giant, compared to which it is about 2.5 mag fainter. The clump giant is separated from the source by about 400 mas, so it is unlikely to be associated with the event. However, it does prevent us from placing any useful limits on the lens light.

From Table 5, it would appear that ρ is measured with tolerable precision, albeit with substantially different error bars for the two solutions. However, the $\chi^2(\rho)$ function is highly non-Gaussian (i.e., not even approximately quadratic). Rather, for, e.g., the close solution, it is approximately flat for $0.003 \lesssim \rho \lesssim 0.0045$, rising linearly, $\Delta\chi^2 \simeq 12-4000\rho$ at lower values, and rising almost vertically at higher values. If we simply adopt the best-fit $\rho \sim 3.6 \times 10^{-3}$, then $\theta_{\rm E} \simeq 0.42\,{\rm mas}$ and $\mu_{\rm rel} \simeq 4.8\,{\rm mas\,yr^{-1}}$. However, because somewhat lower values of ρ (hence, higher $\mu_{\rm rel}$, which are kinematically favored by Galactic models) have a minimal χ^2 penalty, we will use the actual $\chi^2(\rho)$ function in the Bayesian analysis of Section 5.4, rather than the Gaussian approximation.

4.5. KMT-2018-BLG-2602

Very similarly to the case of OGLE-2018-BLG-0298 (Section 4.4), the source is blended with a clump giant, although in this case the source is 1.5 mag fainter. In addition, in this case, the source is aligned with the baseline object to within 10 mas, probably indicating that the (clump-giant) blend is a companion to the (sub-giant) source. If one were to naively apply the arguments given above for KMT-2018-BLG-0030 and KMT-2018-BLG-0087, one might conclude from the presence of a clump-giant blend that no useful limits could be put on lens light. However, this proves not to be the case (see Section 5.5).

In Table 6, we list a $2.5\,\sigma$ limit $\rho < 0.074$, which considered by itself would imply $\mu_{\rm rel} > 0.13\,{\rm mas\,yr^{-1}}$, i.e., completely unconstraining according to Equation (8). We check whether there are are additional subtle structures in the $\chi^2(\rho)$ function that might provide additional constraints. However, we find, on the contrary, that all values $0 < \rho < 0.05$ are consistent with the minimum at $1\,\sigma$. Hence, we simply adopt the Table 6 $2.5\,\sigma$ limit in the

Bayesian analysis in Section 5.5.

For completeness, we note that *Gaia* lists a proper-motion measurement for the baseline object of $\boldsymbol{\mu}_{\rm base}(N,E) = (-9.89 \pm 0.12, -2.37 \pm 0.19)\,{\rm mas\,yr^{-1}}$. If, as appears very likely, the baseline object is composed of the source and its companion, then the source proper motion is given by $\boldsymbol{\mu}_S = \boldsymbol{\mu}_{\rm base}$. This source proper motion would then be about $|\Delta\boldsymbol{\mu}| \sim 4.7\,{\rm mas\,yr^{-1}}$, i.e., 1.6σ from the bulge mean. However, we do not include this measurement in the analysis for two reasons. First, we cannot be certain that the blend is a companion to the source. Second, in the absence of significant constraints on $\mu_{\rm rel}$, knowledge of the source proper motion plays very little role.

4.6. OGLE-2018-BLG-1119

OGLE-2018-BLG-1119 is one of only two events that are analyzed in this paper that are covered by OGLE-III. We therefore provide calibrated photometry for it in Figure 11 and in Table 11.

Moreover, this also allows us to compare the field-star astrometry of pyDIA KMTC to that of OGLE-III. Both catalogs find a neighbor roughly due east of the source, at about 760 mas for OGLE-III and 870 mas for KMTC. However, the two catalogs divide the light between these two stars differently: OGLE-III puts 75% of the total light in the source, whereas for KMTC, this figure is 33%. Furthermore, the combined light of the two stars is 0.32 mag brighter in KMTC (after alignment of the two systems).

From this comparison, we can robustly conclude that the baseline object is semi-resolved from its neighbor, but we cannot tell, a priori, whether OGLE-III or KMTC has a more accurate assessment of the brightness of the baseline object. Nevertheless, it is striking that the KMTC baseline-object measurement is nearly identical to the source flux as determined from the light-curve model, implying that it is quite possible that there is very little blended light, e.g., from the lens. Therefore, we do not show any blend in the CMD.

On the other hand, we cannot rule out that the OGLE-III measurement is actually correct. Therefore, we must place a conservative limit on lens light, namely that $I_L > 19.7$, i.e., roughly as bright as the source.

In Table 7, we show only an upper limit for the ρ measurement. This is because, while there is a clearly defined minimum in $\chi^2(\rho)$ at the $1\,\sigma$ level, all values $\rho < 0.065$ are consistent at $\Delta\chi^2 < 4$. If we, for the moment, take the best fit value $\rho = 0.045$ seriously, then $t_* = 1.84\,{\rm days}$, so that $\mu_{\rm rel} = \theta_*/t_* = 0.14\,{\rm mas\,yr^{-1}}$, which is extraordinarily

unlikely according to Equation (8). Therefore, the apparent 1-σ "measurement" of ρ is almost certainly due to a statistical fluctuation or minor systematics. Hence, in Section 5.6, we use only the upper limit $\rho < 0.071$ (or $\rho < 0.061$).

4.7. KMT-2018-BLG-0173

Recall from Section 3.8 that it was difficult to distinguish among three possibilities: 2L1S (close), 2L1S (wide), and 1L2S. In brief, 2L1S (close) was preferred over the other two by $\Delta\chi^2 \sim 11$. Moreover, both the 2L1S (wide) and 1L2S solutions had reasonably well-determined ρ values that would imply improbably low values of $\mu_{\rm rel}$. Note that the best fit value for θ_* given in Table 11 is (as always) for the lowest-χ^2 solution. Hence, $\theta_{*,\rm wide} = \theta_{*,\rm close} \times 10^{0.48/5} = 5.45\,\mu$as.

Nevertheless, we found that these proper-motion arguments could be evaded in both cases by accepting a modest χ^2 penalty for enforcing $\rho = 0$, which would thereby accommodating much higher (including very plausible) proper motions.

An additional color-based argument was given against 1L2S, but unfortunately this was statistically weak; $\Delta\chi^2 = 2.5$.

Here, we show that the CMD, when combined with the astrometric measurements, argues in exactly the opposite direction, i.e., that both the 2L1S (wide) and 1L2S solutions are strongly preferred over the 2L1S (close) solution.

The argument concerns the blended light. The first point is that in the 2L1S (close) solution, the blended light is about equal to that of the source, while in both the 2L1S (wide) and 1L2S solutions, the blended light is consistent with zero at $1\,\sigma$. This difference becomes important because the measured offset between the source and the baseline object is just 7 mas, i.e., within the measurement error. This close alignment implies that the blended light (if any) is almost certainly associated with the lens, either the lens itself, a companion to the lens, or a companion to the source. (The usual argument against field-star contamination is made even stronger by the fact that the surface density of clump stars (which are proxies for the giant stars of direct interest here) is only half that of Baade's Window, and so a factor 3–5 smaller than that of typical events[2].)

Figure 10 shows the source and blend positions for the 2L1S close solution in blue and

[2]We evaluate this using the measurements by Nataf et al. (2013) in the neighborhood of the reflection point $(l, b) \rightarrow (l, -b)$ because the northern bulge is not well covered in that study.

green, respectively. The magenta point shows the baseline object, which would be the source position for either of the other solutions, assuming no blending. Thus, in the 2L1S close solution (but for neither of the others), the blend would be (within measurement error) a twin of the source, and thus almost certainly a companion to the source of virtually identical mass in a very rapid phase of stellar evolution.

Because each of these three solutions has some very improbable feature, we do not regard it as possible to confidently choose among them based on current evidence. It is possible that additional data, such as AO imaging and/or spectroscopy on large telescopes, will eventually resolve the issue. However, at present, we believe that this event should not be cataloged as "planetary".

4.8. KMT-2018-BLG-1497

In Section 3.9, we showed that there are three different planetary solutions for KMT-2018-BLG-1497, with mass ratios, q, spanning two orders of magnitude, plus a 1L2S solution, all within $\Delta\chi^2 \lesssim 4$. Thus, the θ_* evaluation in Table 11 and the CMD in Figure 11 (both, as usual, for the lowest-χ^2 solution), are shown only for completeness: they could become of interest if future observations can distinguish among these solutions.

4.9. KMT-2018-BLG-1714

In Section 3.10, we showed that for KMT-2018-BLG-1714, there is a 1L1S solution within $\Delta\chi^2 < 1$ of the best planetary solution. In addition, there was a factor 3.5 degeneracy in q at $\Delta\chi^2 \sim 7$. Thus, as for KMT-2018-BLG-1497, the θ_* evaluation in Table 11 and the CMD in Figure 11 are shown only for completeness because they could become of interest if future observations can distinguish among these solutions.

5. Physical Parameters

To make Bayesian estimates of the lens properties, we follow the same procedures as described in Section 5 of Gould et al. (2022). We refer the reader to that work for details.

In Table 12, we present the resulting Bayesian estimates of the host mass $M_{\rm host}$, the planet mass $M_{\rm planet}$, the distance to the lens system D_L, and the planet-host projected separation $a_\perp$. For the majority of events, there are two or more competing solutions. For

these cases (following Gould et al. 2022), we show the results of the Bayesian analysis for each solution separately, and we then show the "adopted" values below these. For $M_{\rm host}$, $M_{\rm planet}$, and D_L, these are simply the weighted averages of the separate solutions, where the weights are the product of the two factors at the right side of each row. The first factor is simply the total weight from the Bayesian analysis. The second is $\exp(-\Delta\chi^2/2)$ where $\Delta\chi^2$ is the χ^2 difference relative to the best solution. For $a_\perp$, we follow a similar approach provided that either the individual solutions are strongly overlapping or that one solution is strongly dominant. If neither condition were met, we would enter "bi-modal" instead. However, in practice, this condition is met for all 4 events for which there is potentially an issue.

We present Bayesian analyses for 6 of the 9 events, but not for KMT-2018-BLG-0173, KMT-2018-BLG-1497, and KMT-2018-BLG-1714, for which we cannot distinguish between competing interpretations of the event. See Sections 3.8, 3.9, and 3.10. Figures 12 and 13 show histograms for $M_{\rm host}$ and D_L for these 6 events.

5.1. KMT-2018-BLG-0030

For KMT-2018-BLG-0030, there is only one light-curve solution. As discussed in Sections 3.2 and 4.1, while we include two constraints, $t_{\rm E} = 27.94 \pm 0.11$ days and $\theta_{\rm E} > 76\,\mu$as, only the first of these has practical importance.

As illustrated by Figure 12, the relatively long timescale somewhat favors more massive hosts, but the lens-distance distribution primarily just reflects the Galactic prior.

5.2. KMT-2018-BLG-0087

For KMT-2018-BLG-0087, there are two solutions. For each, there are two constraints, one on $t_{\rm E}$ (as given in Table 3) and the other on $\theta_{\rm E}$. As discussed in Section 3.3, the seemingly crude limit on ρ is significant due to the short $t_{\rm E}$. Therefore, as discussed in Section 3.3, the profile $\chi^2(\rho)$ actually matters. Therefore, we implement the $\theta_{\rm E}$ constraint by, for each simulated event with Einstein radius $\theta_{\rm E}$, first evaluating $\rho = \theta_*/\theta_{\rm E}$ (where $\theta_* = 9.53\,\mu$as), and then assigning a weight

$$w_{\theta_{\rm E}} = \frac{\exp[-\chi^2(\rho)/2]}{Q}; \qquad Q \equiv \int_0^\infty d\rho \exp[-\chi^2(\rho)/2], \tag{12}$$

where

$$\chi^2_{\rm inner}(\rho) = \left(\frac{\rho}{0.044}\right)^2;$$

$$\chi^2_{\rm outer}(\rho) = \Bigl(\frac{\rho}{0.080}\Bigr)^2 \quad (\rho < 0.09); \qquad \chi^2_{\rm outer}(\rho) = \frac{81}{64} + 5\Bigl(\frac{\rho - 0.09}{0.02}\Bigr)^2 \quad (\rho > 0.09), \quad (13)$$

with $Q_{\rm inner} = 0.044\sqrt{\pi/2} = 0.055$, and $Q_{\rm outer} = 0.081$.

The host mass is peaked near the star/brown-dwarf boundary, while the lens distance is strongly dominated by the bulge population. See Figure 12. The physical reason for this is that the combination of the modeling constraints and the Galactic priors strongly favors events with small $\theta_{\rm E} = \sqrt{\kappa M \pi_{\rm rel}}$ (so, low M and low $\pi_{\rm rel}$). That is, by itself, the $2.5\,\sigma$ limit on ρ would only imply a lower limit: $\theta_{\rm E} > 0.086\,{\rm mas}$, but substantially larger $\theta_{\rm E}$ would lead to high proper motions that are heavily disfavored by the Galactic priors.

5.3. KMT-2018-BLG-0247

For KMT-2018-BLG-0247, there are two solutions. For each, there are three constraints: the first on $t_{\rm E}$ (as given in Table 4), the second on $\theta_{\rm E}$ (as given in Equations (10) and (11)), and the third on lens light $I_{L,{\rm pyDIA}} > 20.46$ (as described in Section 4.3). In order to put this limit on a calibrated scale, we estimate $I_{\rm calib} - I_{\rm pyDIA} = I_{\rm cl,calib} - I_{\rm cl,pyDIA} = I_{\rm cl,0} + A_I - I_{\rm pyDIA} = -0.03$, where $I_{\rm cl,0}$ and $I_{\rm pyDIA}$ are from Table 11 and $A_I = 2.99$ is from the KMT webpage as described in Section 3.2. Therefore, the calibrated limit is $I_L > 20.43$.

The host distributions (Figure 12) are dominated by bulge M dwarfs. Kim et al. (2021b) showed that for measured proper motions $\mu_{\rm rel} \lesssim 10\,{\rm mas\,yr^{-1}}$, Bayesian mass estimates depend almost entirely on the $\theta_{\rm E}$ measurement. Our results for both the close and wide solutions (which differ by a factor 1.3) are in good accord with the predictions from their Figures 6 and 7. Note that, as anticipated in Section 4.3, the lens flux constraint plays almost no role because the other constraints already favor very faint lenses.

5.4. OGLE-2018-BLG-0298

For OGLE-2018-BLG-0298, there are two solutions. For each, there are three constraints. The first, on $t_{\rm E}$, is given in Table 5, while each of the other two, on $\theta_{\rm E}$ and $\boldsymbol{\pi}_{\rm E}$, require additional discussion.

As mentioned in Section 4.4, for the close solution, $\chi^2(\rho)$ is both fairly broad and highly non-Gaussian. Therefore, as in the case of KMT-2018-BLG-0087 (Section 5.2) we employ Equation (12) by directly characterizing $\chi^2(\rho)$

$$\chi^2_{\rm close}(\rho) = 12 - 4000\rho \quad (\rho < 0.003); \quad = 0 \quad (0.003 < \rho < 0.0045); \quad = 24000\rho - 108 \quad (\rho < 0.0045),$$

$$\chi^2_{\rm wide}(\rho) = \left(\frac{1000\rho - 3.98}{0.48}\right)^2; \tag{14}$$

with $Q_{\rm close} = 2.09 \times 10^{-3}$, and $Q_{\rm wide} = \sqrt{2\pi}0.48 \times 10^{-3} = 1.20 \times 10^{-3}$.

To incorporate the parallax measurement, we could in principle double the number of solutions from 2 to 4, and then average together the Bayesian results from the two close solutions and from the two wide solutions. However, inspection of the parallax solutions given in Section 3.5 (in principal-axis format), shows that the pair of close (or wide) solutions differ by much less than their errors, and the error ellipses are also extremely similar. These are natural consequences of the fact that $u_0 \ll 1$. Hence, it make more sense to average these solutions, before applying the Bayesian results than after. Next, we notice that the parallax solutions for the close and wide solutions for a given sign of u_0 are even more similar than are, e.g., the two close solutions. Hence, for simplicity, we simply average together the four solutions (in equatorial coordinates) to obtain

$$a_{i,0} = \begin{pmatrix} \pi_{{\rm E},N,0} \\ \pi_{{\rm E},E,0} \end{pmatrix} = \begin{pmatrix} -0.1433 \\ +0.0079 \end{pmatrix}; \qquad c_{ij} = \begin{pmatrix} 0.4287 & 0.0127 \\ 0.0127 & 0.0128 \end{pmatrix}, \tag{15}$$

and then derive the parallax weight,

$$w_{\rm par} = \frac{\exp(-\sum_i \sum_j (a_i - a_{i,0}) b_{ij} (a_j - a_{j,0})/2)}{\sqrt{2\pi {\rm det(b)}}}, \tag{16}$$

where $b \equiv c^{-1}$ and $a_i = (\pi_{{\rm E},N}, \pi_{{\rm E},E})_i$ of simulated event, i.

The results of the Bayesian analysis can be qualitatively understood by considering a "typical" value of $\rho \sim 4 \times 10^{-3}$, hence $\theta_{\rm E} \sim 0.38\,{\rm mas}$ and $\mu_{\rm rel} \sim 4\,{\rm mas\,yr^{-1}}$. If there were no parallax information, then the argument of Kim et al. (2021b) would lead to a mass estimate $M \sim 0.44 M_\odot$, with most lenses in the bulge. At typical bulge $\pi_{\rm rel} \sim 16\,\mu{\rm as}$, lenses at this peak mass would have $\pi_{\rm E} \sim 0.07$, which is quite compatible with the parallax constraints. However, at a factor 2 below this peak, the parallax constraint $|\pi_{{\rm E},\parallel}| \lesssim 0.11$ starts to suppress many simulated events. Hence, the mass peak in Figure 13 is shifted higher relative to the Kim et al. (2021b) prediction.

5.5. KMT-2018-BLG-2602

As discussed in Section 3.6, we consider that its $\Delta\chi^2 = 10.3$ preference decisively resolves the degeneracy in favor of the outer solution. When we initially carried out the Bayesian analysis, we considered that there were only two constraints, one on $t_{\rm E} = 99 \pm 14\,{\rm day}$ (given by Table 6) and the other (from Tables 6 and 11), $\theta_{\rm E} > 0.043\,{\rm mas}$. Moreover, as discussed

in Section 3.6, the latter has almost no impact and is included only for completeness. In particular, we did not consider as relevant the fact that the lens must be fainter than the clump-giant blend. However, the resulting lens-distance histogram, which was qualitatively similar to the finally adopted one that is shown in Figure 13, contained a substantial fraction of nearby lenses that, at least potentially, might be excluded by even such a weak constraint. We therefore calibrated the pyDIA measured blend flux $[(V-I), I]_B = (2.99, 16.86)$ to obtain $I_L > 16.82$ and $V_L > 19.57$, using the same procedures as in Section 5.3. For this purpose, we used $A_I = 2.32$ from the KMT webpage and $E(V-I) = A_I/1.10$, estimated from Figure 6 of Nataf et al. (2013). We find that these constraints have a small, but non-negligible effect, as we quantify below.

The bi-modal distance distribution in Figure 13, can be understood as follows. For typical $\mu_{\rm rel} \sim 6\,{\rm mas\,yr^{-1}}$, $\sqrt{\kappa M \pi_{\rm rel}} = \theta_{\rm E} = \mu_{\rm rel} t_{\rm E} \sim 1.7\,{\rm mas}$, which implies massive, nearby lenses, e.g., $M = 0.7\,M_\odot$, $D_L = 1.6\,{\rm kpc}$. Hence, a large number of simulated disk events are consistent with this timescale. On the other hand proper motions that are, e.g., 5 times slower, so $\theta_{\rm E} \sim 0.33$ mas would be consistent with massive lenses in the bulge. Such low proper motions are somewhat disfavored, but this is compensated by the high surface density of bulge stars compared to disk stars. Note, however, that in both cases, relatively massive lenses are favored, as shown in the left panel.

As noted above, before including the lens-flux constraints, the Bayesian priors would favor large $\theta_{\rm E}$ and hence massive, nearby lenses. Specifically, we find that this suppression of nearby disk lenses reduces the median value of $M_{\rm host}$ by 10% relative to the case of no flux constraint, while the median value of D_L is increased by 8%.

5.6. OGLE-2018-BLG-1119

For OGLE-2018-BLG-1119, there are two solutions. For each, there are three constraints: the first on $t_{\rm E}$ (as given in Table 7), the second on $\theta_{\rm E}$ (as derived from Tables 7 and 11), i.e., $\theta_{\rm E,inner} > 0.062\,{\rm mas}$ and $\theta_{\rm E,outer} > 0.063\,{\rm mas}$, and the third on lens light $I_L > 19.7$ (as described in Section 4.6). We note that this limit is already on the OGLE-III calibrated scale.

As in the case of KMT-2018-BLG-2602, the distance distribution is bi-modal, and the explanation for this is similar: the event has a relatively long $t_{\rm E} \sim 40\,{\rm days}$ and there is only an extremely weak constraint on $\theta_{\rm E}$. However, following the logic of Section 5.5 and noting that the timescale is significantly shorter than in that case, we expect the disk peak to be weaker and the bulge peak to be stronger, while we expect the median mass to be

significantly lower. All these expectations are confirmed by Figure 13 and Table 12.

.

6. Discussion

6.1. Summary of 2018 AnomalyFinder Detections

The main goal of this paper has been to complete the 2018 AnomalyFinder sample, with the ultimate purpose being to lay the basis for a mass-ratio function analysis. We summarize this work in Table 13, where we combine the results on the 9 planetary (or possibly planetary) events analyzed here with 10 previously published such events that were identified by the AnomalyFinder algorithm. We have divided these into 14 events that are likely to survive final selection for mass-ratio studies and 5 that are unlikely to survive. However, in this paper we do not give final designations for individual events but, rather, provide the necessary information for others to do so. In Table 13, we indicate when there are multiple solutions and give the $(\log q, s)$ of the lowest χ^2 solution. In future mass-ratio studies, it will be necessary to define a best-representative $\log q$ and to exclude events for which the different solutions are too divergent to do so.

We note that one previously published planetary event, OGLE-2018-BLG-1996, was identified by the AnomalyFinder algorithm but was not selected in the by-eye review. This is one of only two such cases out of all previously published planets from 2016-2019 that were recovered by the AnomalyFinder algorithm. Because the number of such failures is small, they do not generate a significant systematic effect. We therefore believe that this event should be included in the mass-ratio function sample. Again, however, it is not the purpose of this paper to make a final decision on this issue.

Table 13 should be compared to Table 14 of Gould et al. (2022), which contains a total of 26 planetary (or possibly planetary) events. Three of those events (below the double line) are clearly unsuitable for mass-ratio studies. In addition, as noted by Gould et al. (2022), the OGLE-2018-BLG-1700 planet was discovered in a binary system, which makes it subject to different selection biases. Further, the 1L2S/2L1S degeneracy of OGLE-2018-BLG-1544 are likely to be too severe to include it, while the mass-ratio uncertainties of OGLE-2018-BLG-1025 and OGLE-2018-BLG-1126 are too severe to include them. Hence, it is plausible that a total of approximately 33 (14 sub-prime-field and 19 prime-field planets) will be available from 2018 alone for mass-ratio studies. This would be the largest microlensing planet sample to date.

6.2. 6-D Distribution

In Figure 14, we show a six-dimensional (6-D) representation of these 33 planets, including 2 continuous dimensions (given by the axes) and 4 discrete dimensions that are represented by colors and point types. The abscissa and ordinate are $\log q$ and $I_{S,\rm anom} \equiv I_S - 2.5 \log[A(u_{\rm anom})]$, with the latter being the source brightness in the unperturbed event at the time of the anomaly. Planets from the prime fields are marked in primary colors (red and blue), while planets from the sub-prime fields are marked in non-primary colors (orange and cyan). Planets that were discovered by AnomalyFinder are marked in reddish colors (red and orange), while those previously identified by eye are marked in bluish colors (blue and cyan). Planets with major-image anomalies are shown as triangles, those with minor-image anomalies are shown as circles, while the two that cannot be classified as either (KMT-2018-BLG-0247 and OGLE-2018-BLG-0740) are shown as squares. Events for which the source crossed a caustic are shown as filled symbols, while those for which it did not are shown as open symbols.

The most striking feature of this diagram is the apparent threshold of AnomalyFinder detection at $I_{S,\rm anom} = 18.75$, with one major exception (OGLE-2018-BLG-0962) and one minor exception (KMT-2018-BLG-2718), both being relatively high-q planets. Another very striking feature is the paucity of by-eye detections of non-caustic-crossing events (open bluish symbols) at low-q: i.e., 1 (OGLE-2018-BLG-1185) out of 5 for $\log q < -3$ compared to 7 out of 12 for $\log q > -3$. It is also notable that among the 16 caustic-crossing events, all but two were discovered by eye. Moreover, both of the AnomalyFinder discoveries (OGLE-2018-BLG-0383 and OGLE-2018-BLG-0977) were in prime fields and at $\log q < -3$, a regime where machines may do better than people because the relatively weak signals of low-q events are spread out over a greater number of data points. That is, it appears that AnomalyFinder was essential to finding low-q events, both with and without caustic crossings.

Zhu et al. (2014) predicted that roughly half of all planet detections in a KMT-like survey would not have caustic-crossing features. The 2018 AnomalyFinder sample, which has 16 caustic-crossing and 17 non-caustic-crossing events, is consistent with this prediction.

Another anticipated feature of the KMT survey is also confirmed. When KMT began regular observations in 2016, it adopted the layered approach pioneered by OGLE, in which a relatively small region would be monitored at high-cadence (which we call the "prime fields") and much larger regions would be monitored at a series of lower cadences (Kim et al. 2018a). It was expected that the higher-cadence fields would be more sensitive to lower-q planets (Henderson et al. 2014). Figure 14 shows that for $\log q < -3$, 9 of 11 planets are from prime fields (primary colors), compared to 10 out of 22 for $\log q > -3$.

Finally, there are 14 planets with major-image perturbations, compared to 17 with minor-image perturbations, which is statistically consistent with the expectation that these should be about equal.

This research has made use of the KMTNet system operated by the Korea Astronomy and Space Science Institute (KASI) and the data were obtained at three host sites of CTIO in Chile, SAAO in South Africa, and SSO in Australia. This research was supported by the Korea Astronomy and Space Science Institute under the R&D program(Project No. 2022-1-830-04) supervised by the Ministry of Science and ICT. Work by C.H. was supported by the grants of National Research Foundation of Korea (2020R1A4A2002885 and 2019R1A2C2085965). J.C.Y. acknowledges support from US NSF Grant No. AST-2108414. W.Z. and H.Y. acknowledge support by the National Science Foundation of China (Grant No. 12133005).

REFERENCES

Alard, C. & Lupton, R.H.,1998, ApJ, 503, 325

Albrow, M.D. Michaeldalbrow/Pydia: InitialRelease On Github., vv1.0.0, Zenodo

Albrow, M. D., Horne, K., Bramich, D. M., et al. 2009, MNRAS, 397, 2099

Bensby, T. Yee, J.C., Feltzing, S. et al. 2013, A&A, 549, A147

Bessell, M.S., & Brett, J.M. 1988, PASP, 100, 1134

Gaia Collaboration, Prusti, T., de Bruijne, J.H.J., et al. 2016, A&A, 595, A1

Gaia Collaboration, Brown, A. G. A., Vallenari, A., et al. 2018, A&A, 616, 1

Gaudi, B.S. 1998, ApJ, 506, 533

Gaudi, B.S. & Gould, A. 1997, ApJ, 486, 85

Gonzalez, O. A., Rejkuba, M., Zoccali, M., et al. 2012, A&A, 543, A13

Gould, A., Zang, W., Mao, S., & Dong, S., 2021, RAA, 21, 133

Gould, A., Han, C., Zang, W.., 2022, A&A, in press, arXiv: arXiv:2204.04354

Gould, A., Ryu, Y.-H., Calchi Novati, S., et al. 2020, JKAS, 53, 9

Griest, K. & Safizadeh, N. 1998, ApJ, 500, 37

Han, C., Udalski, A., Gould, A., et al. 2016, ApJ, 828, 53

Han, C., Yee, J.C., Udalski, A., et al. 2019, AJ, 158, 102

Han, C., Udalski, A., Kim, D., et al. 2021a, A&A, 650A, 89

Han, C., Albrow, M.D., Chung, S.-J., et al. 2021b, A&A, 652A, 145

Han, C., Gould, A., Albrow, M.D., et al. 2021c, A&A, 658A, 62

Henderson, C.B., Gaudi, B.S., Han, C., et al. 2014, ApJ, 794, 52

Hwang, K.-H., Zang, W., Gould, A., et al.., 2022, AJ, 163, 43

Kervella, P., Bersier, D., Mourard, D., et al. 2004a, A&A, 428, 587

Kervella, P., Thévenin, F., Di Folco, E., & Ségransan, D. 2004b, A&A, 426, 297

Kim, S.-L., Lee, C.-U., Park, B.-G., et al. 2016, JKAS, 49, 37

Kim, D.-J., Kim, H.-W., Hwang, K.-H., et al., 2018a, AJ, 155, 76

Kim, H.-W., Hwang, K.-H., Shvartzvald, Y., et al. 2018b, arXiv:1806.07545

Kim, Y.-H., Chung, S.-J., Udalski, A., et al. 2021a, MNRAS, 503, 2706

Kim, Y.H.., Chung, S.-J., Yee, J.-C., et al. 2021b, AJ, 162, 17

Kubiak, M. & Szymański, M.K. 1997, Acta Astron., 47, 319.

Minniti, D., Lucas, P. W., Emerson, J. P., et al. 2010, New Astron., 15, 433

Minniti, D., Lucas, P., VVV Team, 2017, yCAT 2348, 0

Nataf, D.M., Gould, A., Fouqué, P. et al. 2013, ApJ, 769, 88

Paczyński, B. 1986, ApJ, 304, 1

Park, B.-G., DePoy, D.L.., Gaudi, B.S., et al. 2004, ApJ, 609, 166

Ryu, Y.-H., Hwang, K.-H., Gould, A. et al. 2019, AJ, 158, 151

Ryu, Y.-H., Navarro, M.G., Gould, A. et al. 2020, AJ, 159, 58

Ryu, Y.-H., Hwang, K.-H., Gould, A. et al. 2021, AJ, 162, 96

Ryu, Y.-H., Jung, Y.K., Yang, H., et al. 2022, AJ, submitted, arXiv:2202.03022

Szymański, M.K. 2005, Acta Astron., 55, 43

Szymański, M.K., Udalski, A., Soszyński, I., et al. 2011, Acta Astron., 61, 83

Tomaney, A.B. & Crotts, A.P.S. 1996, au, 112, 2872

Udalski, A. Szymański, M., Kubiak, M., et al., 2002, Acta Astron., 52, 217

Udalski, A. 2003, Acta Astron., 53, 291

Udalski, A.,Szymanski, M., Kaluzny, J., et al. 1994, Acta Astron., 44, 227

Woźniak, P. R. 2000, Acta Astron., 50, 421

Wang, H., Zang, W., Zhu, W, et al. 2022, MNRAS, 510, 1778

Yee, J.C., Gould, A., Beichman, C., 2015, ApJ, 810, 155

Yee, J.C., Zang, W., Udalski, A. et al. 2021, AJ, 162, 180

Yoo, J., DePoy, D.L., Gal-Yam, A. et al. 2004, ApJ, 603, 139

Zang, W., Shvartzvald, Y., Udalski, A., et al. 2019, arXiv:2010.08732

Zang, W., Hwang, K.-H., Udalski, A., et al. 2021b, AJ, 162, 163

Zang, W., Yang, H., Han, c., et al. 2022, arXiv:2204.02017

Zhang, K. & Gaudi, B.S. 2022, arXiv:2205.05085

Zhu, W., Penny, M., Mao, S., Gould, A., & Gendron, R. 2014, ApJ, 788, 73

This preprint was prepared with the AAS LaTeX macros v5.2.

Table 1. Event Names, Cadences, Alerts, and Locations

Name	$\Gamma\,(\mathrm{hr}^{-1})$	Alert Date	$\mathrm{RA_{J2000}}$	$\mathrm{Dec_{J2000}}$	l	b
KMT-2018-BLG-0030	1.0	21 Jun 2018	17:38:04.00	−28:02:29.85	−0.11	+1.88
KMT-2018-BLG-0087	2.0	21 Jun 2018	17:37:18.48	−27:49:55.42	−0.03	+2.14
KMT-2018-BLG-0247	1.0	08 Jul 2018	17:38:14.41	−27:09:01.48	+0.66	+2.33
OGLE-2018-BLG-1219	1.3					
OGLE-2018-BLG-0298	1.0	05 Mar 2018	17:37:08.28	−29:42:32.80	−1.63	+1.16
KMT-2018-BLG-1354	1.0					
KMT-2018-BLG-2602	0.4	Post Season	17:49:35.29	−21:58:34.32	+6.43	+2.83
OGLE-2018-BLG-1119	0.3	22 Jun 2018	18:00:07.02	−32:22:31.0	−1.38	−4.43
KMT-2018-BLG-1870	0.4					
KMT-2018-BLG-0173	0.4	21 Jun 2018	17:50:11.75	−21:35:40.56	+6.83	+2.91
KMT-2018-BLG-1497	1.0	Post Season	17:44:20.19	−25:58:25.00	+2.38	+1.79
KMT-2018-BLG-1714	1.0	Post Season	17:50:27.27	−33:22:33.82	−3.27	−3.17

Table 2. Light Curve Parameters for KMT-2018-BLG-0030

Parameter	
χ^2/dof	2397.43/2388
$t_0 - 8270$	1.459 ± 0.043
u_0 (10^{-2})	90.05 ± 0.15
$t_{\rm E}$ (days)	27.94 ± 0.11
s	1.580 ± 0.013
q (10^{-3})	2.74 ± 0.30
$\langle \log q \rangle$	-2.563 ± 0.048
α (rad)	2.3521 ± 0.0065
ρ (10^{-3})	< 112
$I_{\rm S}$	16.82 ± 0.00

Table 3. Light Curve Parameters for KMT-2018-BLG-0087

Parameter	Inner	Outer
χ^2/dof	3103.66/3087	3098.47/3087
$t_0 - 8280$	1.7373 ± 0.0077	1.7290 ± 0.0079
u_0 (10^{-2})	51.4 ± 1.7	52.8 ± 1.8
$t_{\rm E}$ (days)	4.607 ± 0.088	4.536 ± 0.090
s	0.638 ± 0.014	0.898 ± 0.024
q (10^{-3})	2.73 ± 0.51	2.17 ± 0.46
$\langle \log q \rangle$	-2.569 ± 0.083	-2.668 ± 0.092
α (rad)	5.001 ± 0.012	4.986 ± 0.012
ρ (10^{-3})	< 96	< 110
$I_{\rm S}$	16.86 ± 0.05	16.82 ± 0.05

Table 4. Light Curve Parameters for KMT-2018-BLG-0247

Parameter	Close	Wide
χ^2/dof	4172.76/4854	4171.10/4854
$t_0 - 8300$	8.4239 ± 0.0065	8.4206 ± 0.0062
u_0 (10^{-2})	6.86 ± 0.40	6.51 ± 0.36
$t_{\rm E}$ (days)	10.56 ± 0.47	10.67 ± 0.47
s	0.9720 ± 0.0045	1.1182 ± 0.0048
q (10^{-3})	6.28 ± 0.46	7.11 ± 0.56
$\langle \log q \rangle$	-2.203 ± 0.032	-2.149 ± 0.034
α (rad)	1.146 ± 0.014	1.200 ± 0.010
ρ (10^{-3})	1.92 ± 0.19	2.52 ± 0.26
$I_{\rm S}$	20.95 ± 0.06	20.96 ± 0.06

Table 5. Light Curve Parameters for OGLE-2018-BLG-0298

Parameter	Close	Wide	1L2S
χ^2/dof	3116.68/3258	3119.27/3258	3150.36/3257
$t_0 - 8180$	8.7417 ± 0.0052	8.7387 ± 0.0052	8.7078 ± 0.0048
$t_{0,2} - 8180$			10.646 ± 0.014
u_0 (10^{-2})	2.151 ± 0.077	2.149 ± 0.077	2.317 ± 0.139
$u_{0,2}$ (10^{-2})			0.147 ± 0.094
$t_{\rm E}$ (days)	32.08 ± 0.98	32.28 ± 0.99	33.35 ± 1.11
s	0.957 ± 0.018	1.079 ± 0.016	
q (10^{-3})	0.199 ± 0.045	0.137 ± 0.027	
$\langle \log q \rangle$	-3.705 ± 0.099	-3.861 ± 0.081	
α (rad)	0.350 ± 0.006	0.357 ± 0.005	
ρ (10^{-3})	3.58 ± 0.73	3.98 ± 0.48	< 25.50
ρ_2 (10^{-3})			6.20 ± 0.59
q_F (10^{-3})			13.1 ± 1.4
$I_{\rm S}$	20.67 ± 0.04	20.68 ± 0.04	20.74 ± 0.04

Table 6. Light Curve Parameters for KMT-2018-BLG-2602

Parameter	Inner	Outer	1L2S
χ^2/dof	936.65/920	926.34/920	957.01/919
$t_0 - 8260$	9.95 ± 0.14	10.33 ± 0.15	11.24 ± 0.18
$t_{0,2} - 8260$			-16.59 ± 0.29
u_0 (10^{-2})	56.5 ± 11.4	51.8 ± 9.3	46.9 ± 8.6
$u_{0,2}$ (10^{-2})			0.092 ± 0.513
$t_{\rm E}$ (days)	94.4 ± 16.1	98.7 ± 14.0	108.9 ± 13.7
s	1.532 ± 0.084	1.182 ± 0.065	
q (10^{-3})	1.62 ± 0.25	1.65 ± 0.27	
$\langle \log q \rangle$	-2.794 ± 0.067	-2.782 ± 0.071	
α (rad)	2.033 ± 0.017	2.057 ± 0.015	
ρ (10^{-3})	< 72	< 74	
ρ_2 (10^{-3})			35.8 ± 6.1
q_F (10^{-3})			3.44 ± 0.57
$I_{\rm S}$	17.88 ± 0.33	18.03 ± 0.28	18.21 ± 0.26

Table 7. Light Curve Parameters for OGLE-2018-BLG-1119

Parameter	Inner	Outer	1L2S
χ^2/dof	1205.16/1267	1210.73/1267	1219.17/1266
$t_0 - 8310$	5.98 ± 0.13	6.05 ± 0.13	6.28 ± 0.14
$t_{0,2} - 8310$			0.87 ± 0.16
u_0 (10^{-2})	43.5 ± 5.2	40.5 ± 4.6	43.2 ± 5.4
$u_{0,2}$ (10^{-2})			0.59 ± 0.78
$t_{\rm E}$ (days)	39.3 ± 3.2	41.2 ± 3.3	40.3 ± 3.4
s	1.426 ± 0.047	1.081 ± 0.038	
q (10^{-3})	1.81 ± 0.46	1.70 ± 0.43	
$\langle \log q \rangle$	-2.74 ± 0.11	-2.78 ± 0.11	
α (rad)	1.857 ± 0.016	1.869 ± 0.016	
ρ (10^{-3})	< 71	< 61	
ρ_2 (10^{-3})			34.8 ± 6.8
q_F (10^{-3})			4.2 ± 1.0
$I_{\rm S}$	19.53 ± 0.18	19.64 ± 0.17	19.58 ± 0.19

Table 8. Light Curve Parameters for KMT-2018-BLG-0173

Parameter	Close	Wide	1L2S
χ^2/dof	927.58/921	938.79/921	938.44/921
$t_0 - 8340$	8.74 ± 0.11	8.65 ± 0.11	8.71 ± 0.11
$t_{0,2} - 8340$			-83.74 ± 0.15
u_0 (10^{-2})	62.0 ± 4.1	79.7 ± 5.7	83.0 ± 1.2
$u_{0,2}$ (10^{-2})			1.87 ± 0.89
$t_{\rm E}$ (days)	62.51 ± 2.90	52.17 ± 2.59	50.48 ± 0.37
s	0.478 ± 0.015	2.314 ± 0.082	
q (10^{-3})	1.05 ± 0.17	0.97 ± 0.27	
$\langle \log q \rangle$	-2.981 ± 0.069	-3.021 ± 0.125	
α (rad)	5.7990 ± 0.0114	2.7752 ± 0.0087	
ρ (10^{-3})	< 44	125 ± 19	
ρ_2 (10^{-3})			42.5 ± 7.3
q_F (10^{-3})			1.04 ± 0.15
$I_{\rm S}$	17.46 ± 0.12	16.98 ± 0.14	16.90 ± 0.00

Table 9. Light Curve Parameters for KMT-2018-BLG-1497

Parameter	Inner	Outer	Off-axis Cusp	1L2S
χ^2/dof	2466.85/2457	2463.63/2457	2467.78/2457	2465.74/2456
$t_0 - 8220$	9.22 ± 0.11	9.14 ± 0.11	8.07 ± 0.12	8.98 ± 0.12
$t_{0,2} - 8220$				13.854 ± 0.026
u_0 (10^{-2})	22.1 ± 2.3	21.0 ± 1.8	18.4 ± 1.3	19.2 ± 2.4
$u_{0,2}$ (10^{-2})				0.23 ± 0.14
$t_{\rm E}$ (days)	30.6 ± 2.3	31.9 ± 2.0	34.0 ± 1.9	34.2 ± 2.9
s	1.227 ± 0.019	1.128 ± 0.012	0.928 ± 0.005	
q (10^{-3})	0.75 ± 0.24	0.21 ± 0.07	17.38 ± 2.48	
$\langle \log q \rangle$	-3.127 ± 0.136	-3.684 ± 0.139	-1.763 ± 0.063	
α (rad)	0.971 ± 0.020	0.955 ± 0.019	2.971 ± 0.045	
ρ (10^{-3})	< 8.6	7.8 ± 1.7	< 7.8	
ρ_2 (10^{-3})				< 6.7
q_F (10^{-3})				4.2 ± 1.6
$I_{\rm S}$	20.79 ± 0.13	20.87 ± 0.11	21.03 ± 0.09	21.00 ± 0.15

Table 10. Light Curve Parameters for KMT-2018-BLG-1714

Parameter	Inner	Outer	Off-axis Cusp	1L2S
χ^2/dof	2033.08/2028	2032.94/2028	2040.35/2028	2033.80/2027
$t_0 - 8310$	8.168 ± 0.012	8.170 ± 0.012	8.280 ± 0.015	8.179 ± 0.014
$t_{0,2} - 8310$				8.1047 ± 0.0025
u_0 (10^{-2})	15.7 ± 2.0	16.2 ± 2.2	14.4 ± 1.3	18.9 ± 3.1
$u_{0,2}$ (10^{-2})				0.056 ± 0.184
$t_{\rm E}$ (days)	3.21 ± 0.29	3.17 ± 0.30	3.52 ± 0.22	3.12 ± 0.28
s	1.293 ± 0.038	0.921 ± 0.028	0.974 ± 0.004	
q (10^{-3})	3.97 ± 1.67	3.68 ± 1.74	12.83 ± 2.43	
$\langle \log q \rangle$	-2.40 ± 0.14	-2.43 ± 0.15	-1.89 ± 0.081	
α (rad)	1.693 ± 0.024	1.694 ± 0.024	0.030 ± 0.042	
ρ (10^{-3})	< 15.6	< 16.8	< 10.3	
ρ_2 (10^{-3})				< 12.4
q_F (10^{-3})				13.5 ± 2.6
$I_{\rm S}$	20.56 ± 0.17	20.54 ± 0.17	20.72 ± 0.12	20.50 ± 0.19

Table 11. CMD Parameters

Name	$(V-I)_{\rm S}$	$(V-I)_{\rm cl}$	$(V-I)_{\rm S,0}$	$I_{\rm S}$	$I_{\rm cl}$	$I_{\rm cl,0}$	$I_{\rm S,0}$	θ_* (μas)
KMT-2018-BLG-0030	3.57±0.03	3.49±0.03	1.14±0.04	16.88±0.01	17.40±0.03	14.45	13.93±0.03	8.478±0.526
KMT-2018-BLG-0087	3.98±0.05	3.67±0.03	1.37±0.06	16.97±0.02	17.45±0.03	14.44	13.96±0.05	9.529±0.632
KMT-2018-BLG-0247	3.11±0.06	3.65±0.02	0.52±0.07	21.03±0.03	17.43±0.03	14.41	18.01±0.04	0.641±0.055
OGLE-2018-BLG-0298	4.36±0.06	4.65±0.03	0.77±0.07	20.74±0.03	18.55±0.06	14.53	16.72±0.07	1.513±0.142
KMT-2018-BLG-2602	2.93±0.07	2.93±0.03	1.06±0.08	18.22±0.03	16.60±0.05	14.26	15.88±0.06	3.207±0.310
OGLE-2018-BLG-1119	1.64±0.11	2.00±0.03	0.70±0.12	19.50±0.03	15.73±0.05	14.52	18.29±0.06	0.681±0.095
KMT-2018-BLG-0173	3.01±0.06	3.05±0.03	1.02±0.07	17.67±0.02	16.96±0.08	14.25	14.96±0.08	4.371±0.371
KMT-2018-BLG-1497	3.13±0.10	3.26±0.03	0.93±0.11	20.96±0.03	17.45±0.04	14.36	17.87±0.05	1.110±0.166
KMT-2018-BLG-1714	2.60±0.11	2.41±0.03	1.25±0.12	20.08±0.03	16.25±0.05	14.59	18.42±0.06	1.226±0.114

Note. — $(V-I)_{\rm cl,0} = 1.06$

Table 12. PHYSICAL PROPERTIES

Event	Physical Parameters				Relative Weights	
Models	$M_{\rm host}$ $[M_\odot]$	$M_{\rm planet}$ $[M_{\rm Jup}]$	$D_{\rm L}$ [kpc]	$a_\perp$ [au]	Gal.Mod.	χ^2
KB180030	$0.51^{+0.43}_{-0.31}$	$1.45^{+1.23}_{-0.88}$	$6.48^{+1.28}_{-1.96}$	$4.39^{+2.18}_{-2.40}$	1.00	1.00
KB180087						
Inner	$0.11^{+0.15}_{-0.06}$	$0.32^{+0.43}_{-0.16}$	$6.90^{+1.04}_{-1.16}$	$0.66^{+0.20}_{-0.21}$	0.62	0.07
Outer	$0.10^{+0.14}_{-0.05}$	$0.23^{+0.32}_{-0.12}$	$7.02^{+1.03}_{-1.15}$	$0.87^{+0.24}_{-0.25}$	1.00	1.00
Adopted	$0.10^{+0.14}_{-0.05}$	$0.23^{+0.32}_{-0.12}$	$7.02^{+1.03}_{-1.15}$	$0.87^{+0.24}_{-0.25}$		
KB180247						
Close	$0.35^{+0.31}_{-0.18}$	$2.33^{+2.07}_{-1.18}$	$6.47^{+0.99}_{-1.33}$	$2.11^{+0.43}_{-0.52}$	0.65	0.44
Wide	$0.27^{+0.28}_{-0.14}$	$2.04^{+2.09}_{-1.04}$	$6.84^{+0.99}_{-1.24}$	$2.56^{+0.51}_{-0.58}$	1.00	1.00
Adopted	$0.29^{+0.28}_{-0.14}$	$2.11^{+2.09}_{-1.04}$	$6.76^{+0.99}_{-1.24}$	$2.46^{+0.51}_{-0.58}$		
OB180298						
Close	$0.70^{+0.34}_{-0.30}$	$0.15^{+0.07}_{-0.06}$	$6.49^{+0.95}_{-1.23}$	$2.84^{+0.73}_{-0.80}$	1.00	1.00
Wide	$0.63^{+0.34}_{-0.27}$	$0.091^{+0.049}_{-0.038}$	$6.79^{+0.89}_{-1.07}$	$2.98^{+0.54}_{-0.59}$	0.91	0.27
Adopted	$0.69^{+0.34}_{-0.30}$	$0.14^{+0.07}_{-0.06}$	$6.54^{+0.95}_{-1.23}$	$2.86^{+0.73}_{-0.80}$		
KB182602	$0.66^{+0.42}_{-0.36}$	$1.15^{+0.73}_{-0.63}$	$4.31^{+1.97}_{-1.84}$	$3.81^{+2.96}_{-2.32}$	1.00	1.00
OB181119						
Inner	$0.48^{+0.35}_{-0.28}$	$0.91^{+0.66}_{-0.52}$	$5.76^{+1.43}_{-2.48}$	$4.11^{+2.14}_{-2.58}$	1.00	1.00
Outer	$0.48^{+0.35}_{-0.28}$	$0.86^{+0.62}_{-0.49}$	$5.70^{+1.47}_{-2.48}$	$3.13^{+1.65}_{-1.98}$	0.89	0.06
Adopted	$0.48^{+0.35}_{-0.28}$	$0.91^{+0.66}_{-0.52}$	$5.76^{+1.43}_{-2.48}$	$4.06^{+2.14}_{-2.58}$		

Table 13. AnomalyFinder Planets in KMT Sub-prime Fields for 2018

Event Name	KMT Name	$\log q$	s	Reference
KB180029	KB180029	−4.74	1.00	Gould et al. (2020)
OB180298^{AA}	KB181354	−3.71	0.96	This Work
KB181996^{DD}	KB181996	−2.82	1.46	Han et al. (2021a)
KB182602	KB182602	−2.78	1.18	This Work
OB181428	KB180423	−2.76	1.42	Kim et al. (2021a)
OB181119^{AA}	KB181870	−2.74	0.64	This Work
KB180087^{AA}	KB180087	−2.67	2.17	This Work
OB180799	KB181741	−2.60	1.13	Zang et al. (2019)
KB180030	KB180030	−2.56	1.58	This Work
KB181976^{AA}	KB181976	−2.50	1.23	Han et al. (2021a)
KB181292	KB181292	−2.45	1.36	Ryu et al. (2020)
KB181990^{AA,BB}	KB181990	−2.45	0.96	Ryu et al. (2019)
OB180740^{AA}	KB181822	−2.34	1.26	Han et al. (2019)
KB180247^{AA}	KB180247	−2.15	1.12	This Work
KB181988^{AA,GG}	KB181988	−4.45	1.04	Han et al. (2022c)
KB181497^{AA,CC,GG}	KB181497	−3.68	1.13	This Work
KB180173^{AA,CC}	KB180173	−2.98	0.48	This Work
KB181743^{AA,GG}	KB181743	−2.92	1.05	Han et al. (2021b)
KB181714^{AA,CC,GG}	KB181714	−2.43	0.92	This Work

Note. — Event names are abbreviations for, e.g., KMT-2018-BLG-0029 and OGLE-2018-BLG-0799. AA: s degeneracy. BB: Factor 1.6 q degeneracy. CC: 1L2S/2L1S degeneracy. DD: Not selected in AnomalyFinder review. GG: large q degeneracy.

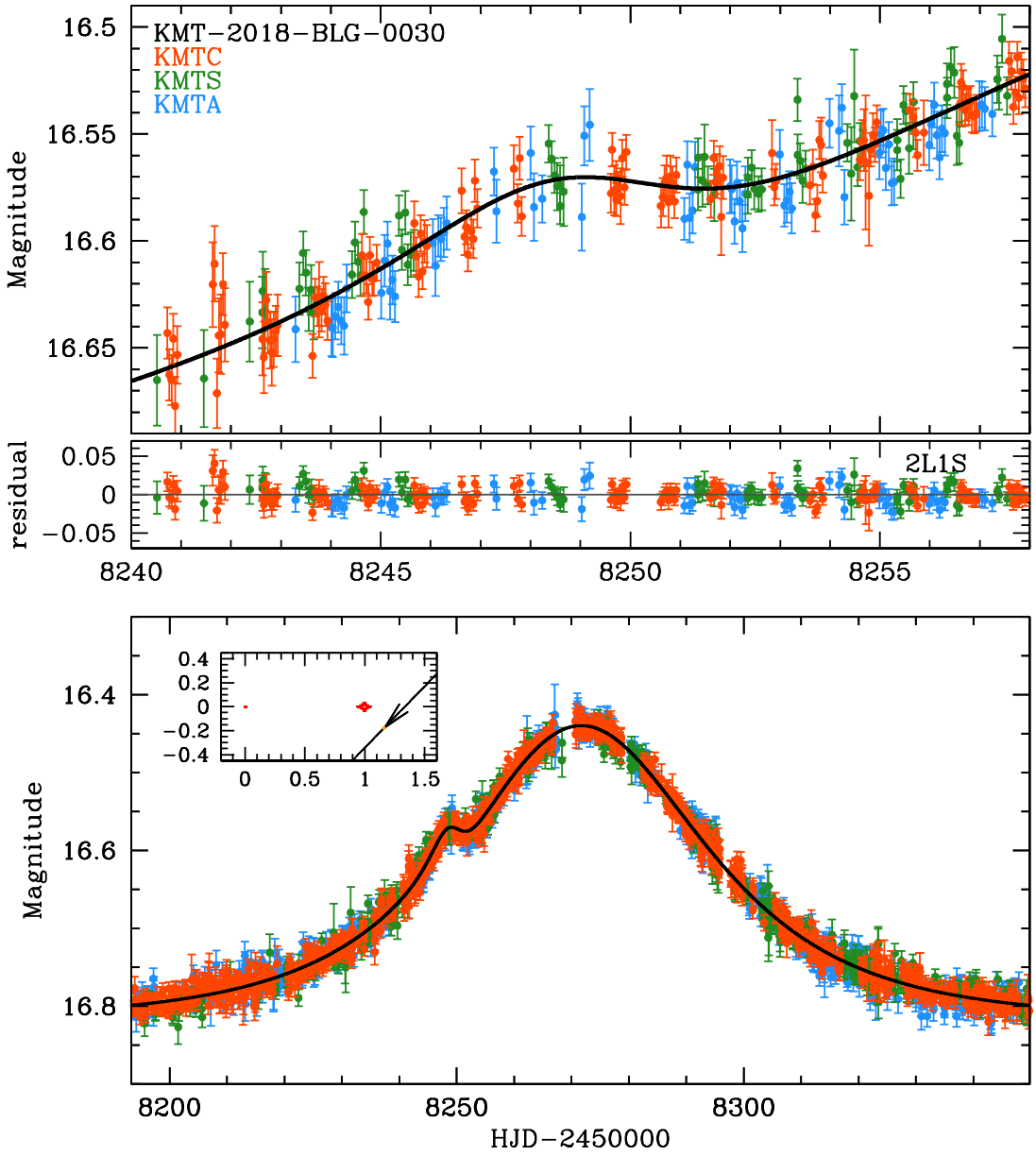


Fig. 1.— Data (color-coded by observatory) together with the prediction and residuals for the model of KMT-2018-BLG-0030 specified in Table 2. The short "bump" at $t_{\rm anom} = 8248.0$ is caused by the source crossing a ridge extending from the planetary caustic due to a $\log q = -2.5$ super-Jovian mass-ratio planet. See inset.

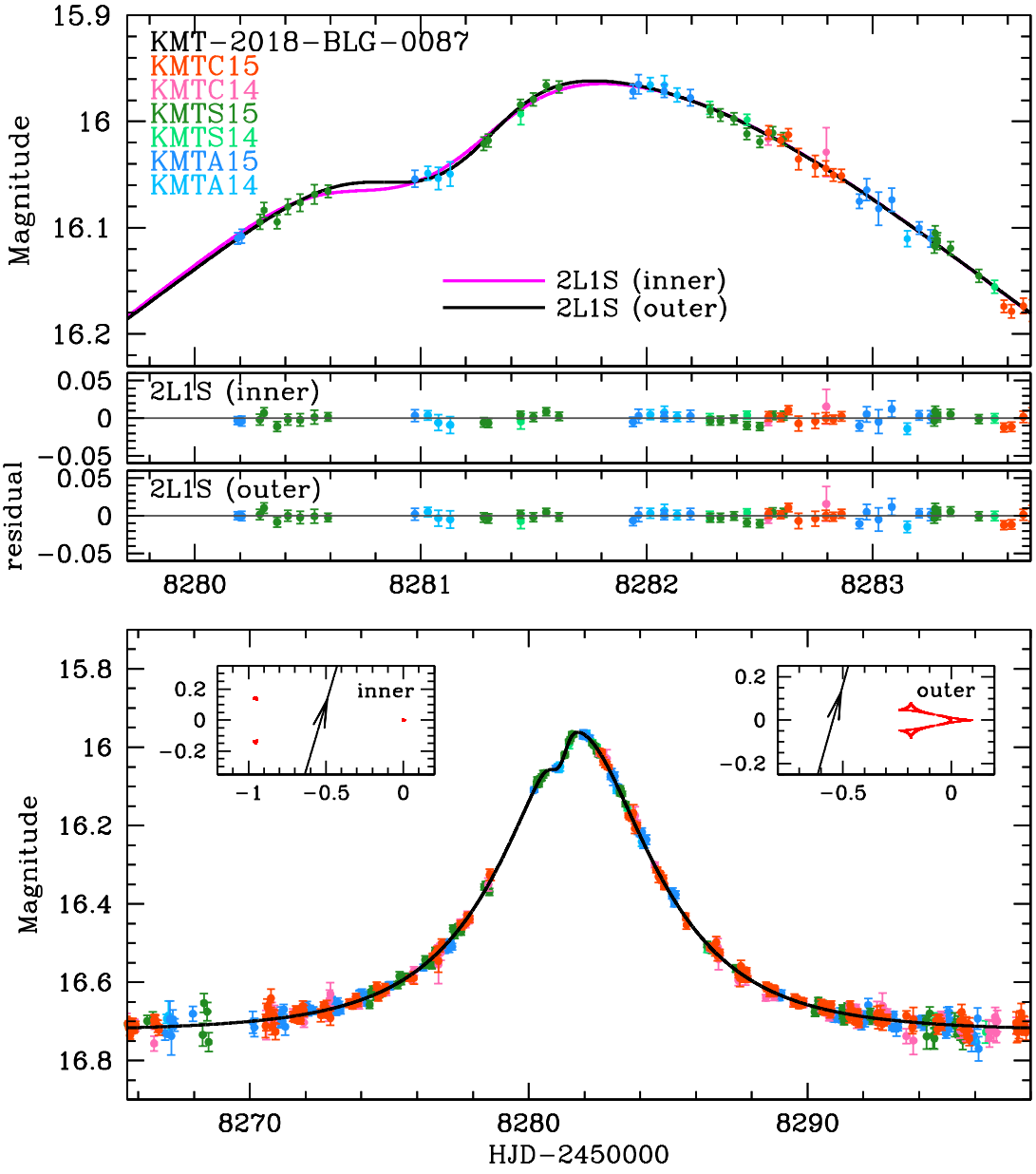


Fig. 2.— Data (color-coded by observatory and field) together with the predictions and residuals for the models of KMT-2018-BLG-0087 specified in Table 3. The short "dip" at $t_{\rm anom} = 8281.73$ is caused by the source crossing the trough that runs along the minor image axis due to a $\log q \sim -2.6$ super-Jovian mass-ratio planet. It is subject to the "inner/outer" degeneracy. See insets.

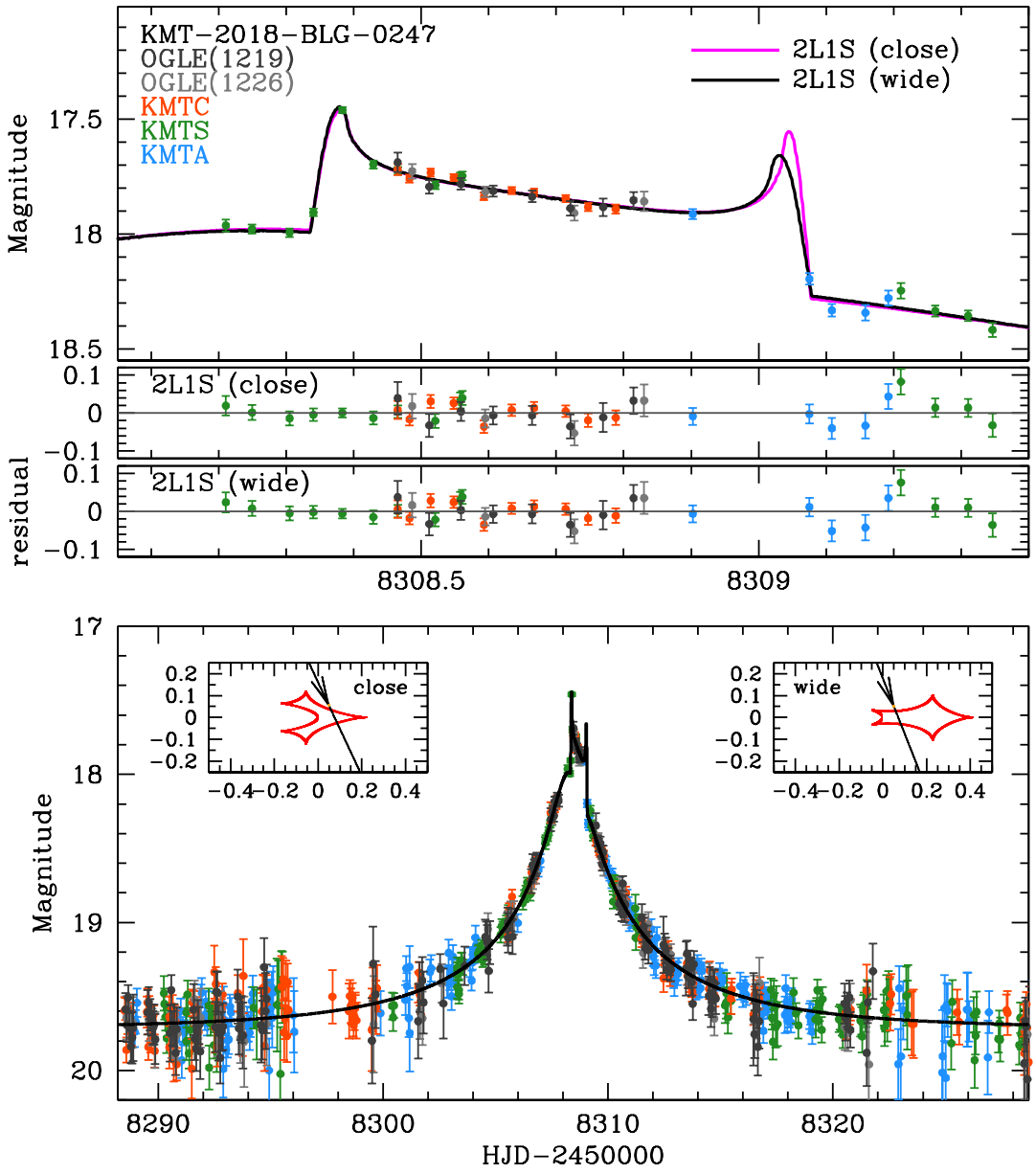


Fig. 3.— Data (color-coded by observatory and field) together with the predictions and residuals for the models of KMT-2018-BLG-0247 specified in Table 4. The "double-horned profile" centered at $t_{\rm anom} = 8305.70$ is caused by the source crossing the main body of a resonant caustic due to a $\log q \sim -2.2$ super-Jovian mass-ratio planet. It is subject to a "close/wide" degeneracy (see insets) due to the lack of data on the caustic exit..

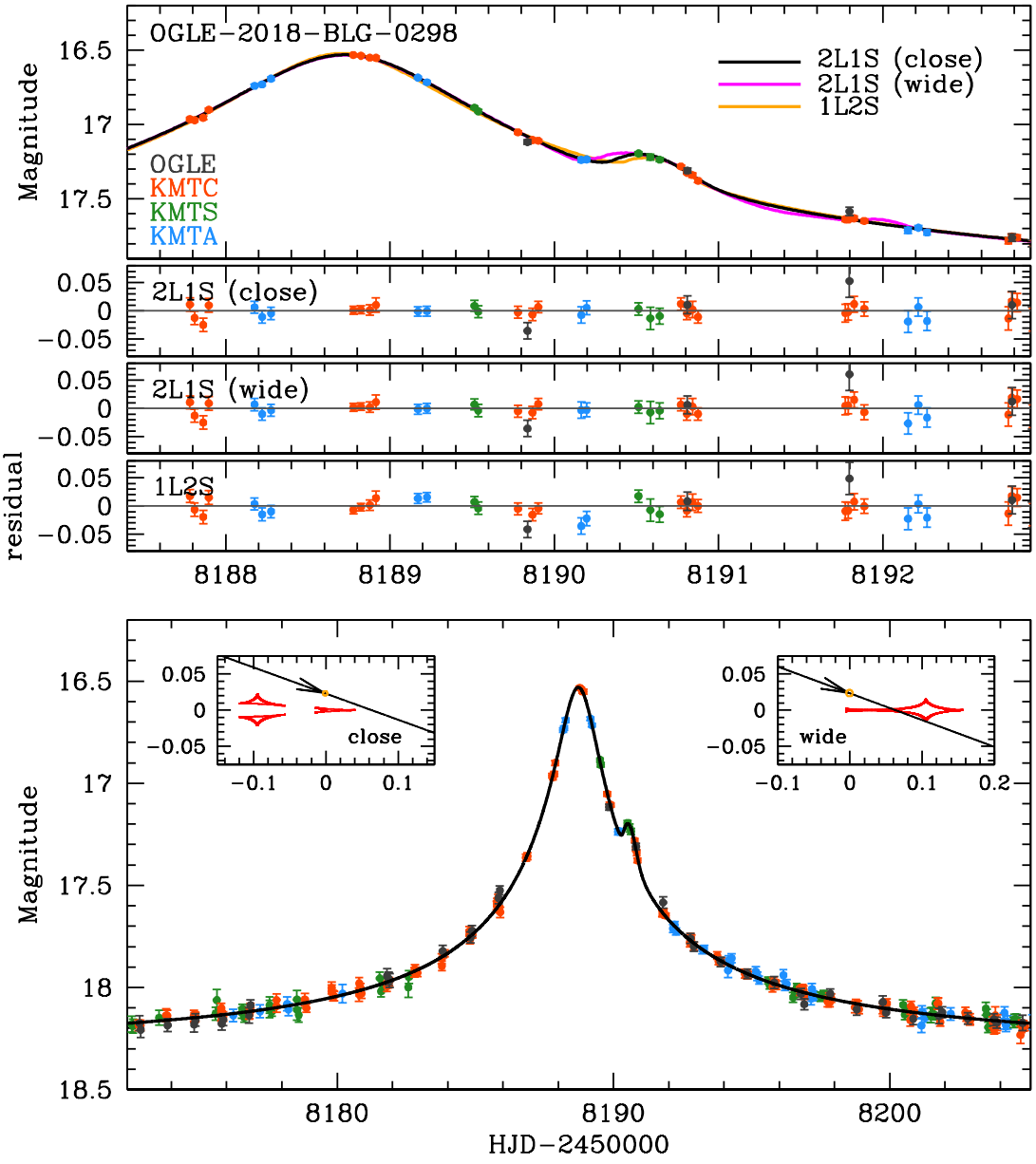


Fig. 4.— Data (color-coded by observatory) together with the predictions and residuals for the models of OGLE-2018-BLG-0298 specified in Table 5. The short "bump" at $t_{\rm anom} = 8190.6$ is caused by the source crossing a ridge in or extending from the major-image side of the caustic structure due to a $\log q \sim -3.7$ sub-Saturn mass-ratio planet. It is subject to a "close/wide" degeneracy. See insets. The 1L2S model is disfavored by $\Delta\chi^2 = 33.7$ and, in addition, is heavily disfavored by kinematic arguments. Hence, it is excluded.

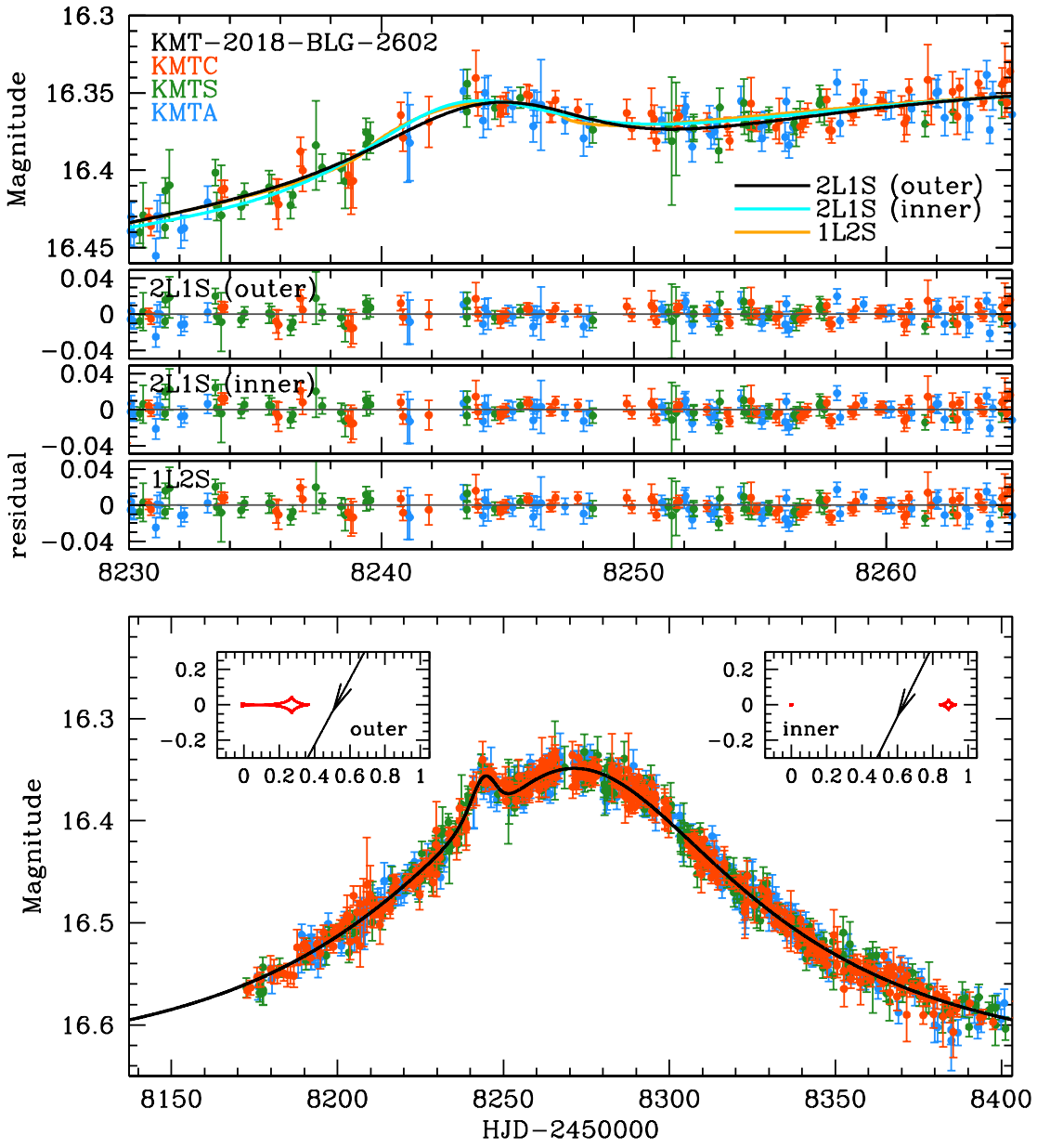


Fig. 5.— Data (color-coded by observatory) together with the predictions and residuals for the models of KMT-2018-BLG-2602 specified in Table 6. The short "bump" at $t_{\rm anom} = 8243.8$ is caused by the source crossing a ridge extending from the planetary caustic (or planetary wing of the resonant caustic) due to a $\log q \sim -2.8$ Jovian mass-ratio planet. It is nominally subject to a "inner/outer" degeneracy (see insets), but we adopt the "outer" solution because it is favored by $\Delta\chi^2 = 10.3$. The 1L2S model is disfavored by $\Delta\chi^2 = 30.7$ and, in addition, is very heavily disfavored by kinematic arguments. Hence, it is excluded.

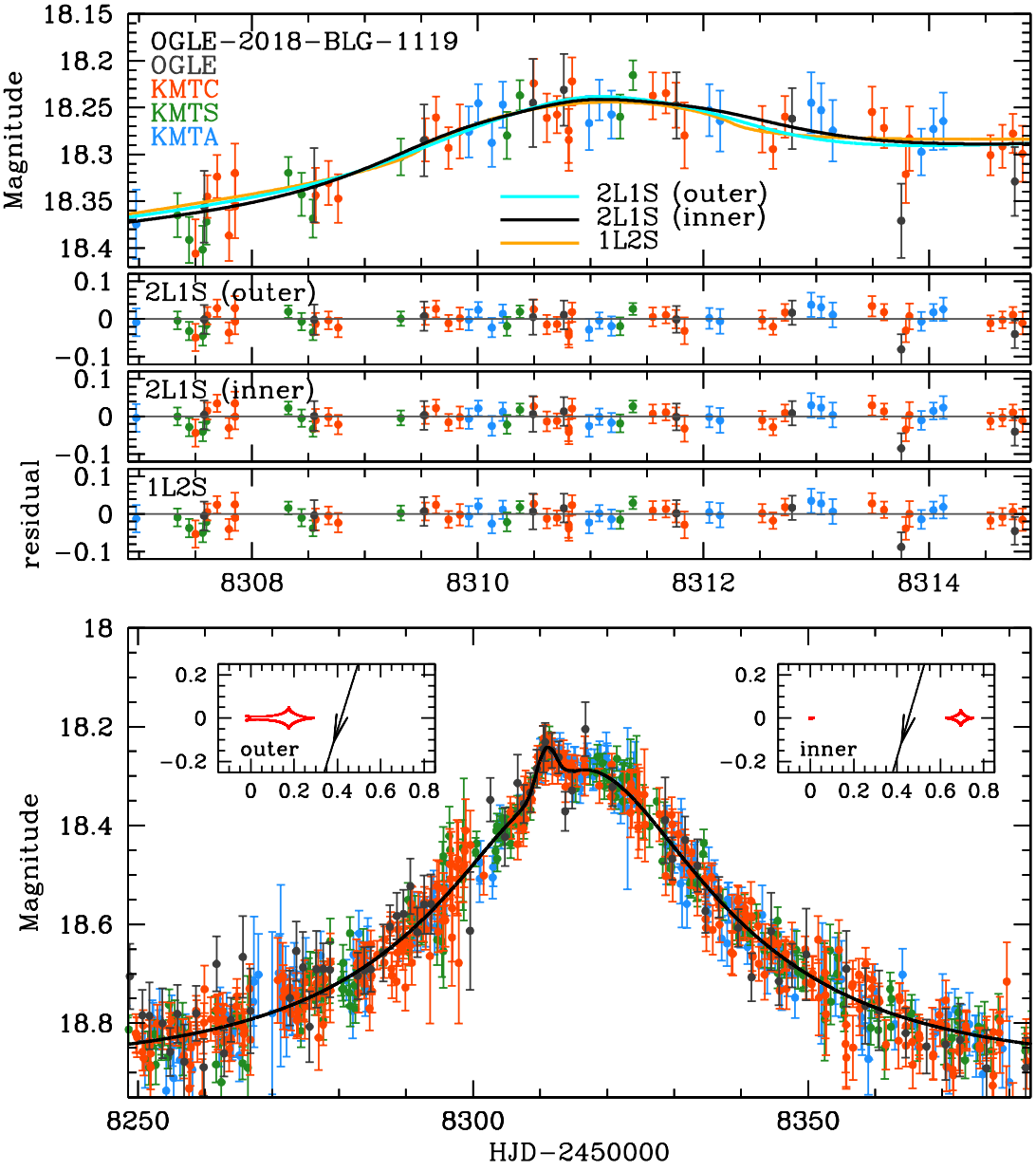


Fig. 6.— Data (color-coded by observatory) together with the predictions and residuals for the models of OGLE-2018-BLG-1119 specified in Table 7. The short "bump" at $t_{\rm anom} = 8310.7$ is caused by the source crossing a ridge extending from the planetary caustic (or planetary wing of the resonant caustic) due to a $\log q \sim -2.75$ Jovian mass-ratio planet. It is subject to a "inner/outer" degeneracy. See insets. The 1L2S model is disfavored by $\Delta\chi^2 = 14.0$ and, in addition, is very heavily disfavored by kinematic arguments. Hence, it is excluded.

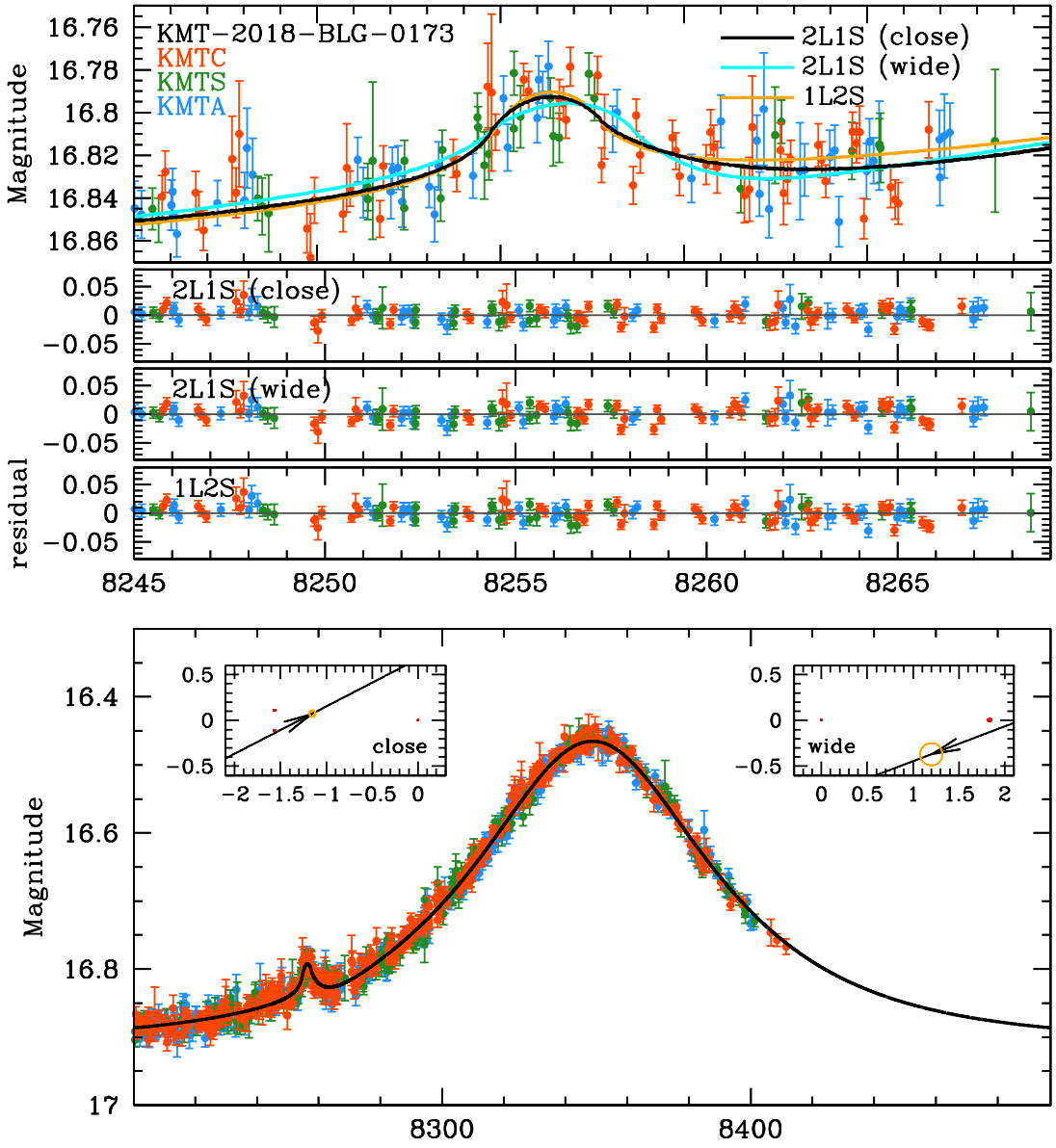


Fig. 7.— Data (color-coded by observatory) together with the predictions and residuals for the models of KMT-2018-BLG-0173 specified in Table 8. The short "bump" at $t_{\rm anom} = 8256$ has 3 possible explanations: source hitting minor image caustic (left inset), source hitting major image caustic (right inset) [both with $\log q = -3.0$], or 1L2S model. The last cannot be decisively rejected based on current data (see Sections 3.8 and 4.7). Therefore, this event should not be cataloged as planetary.

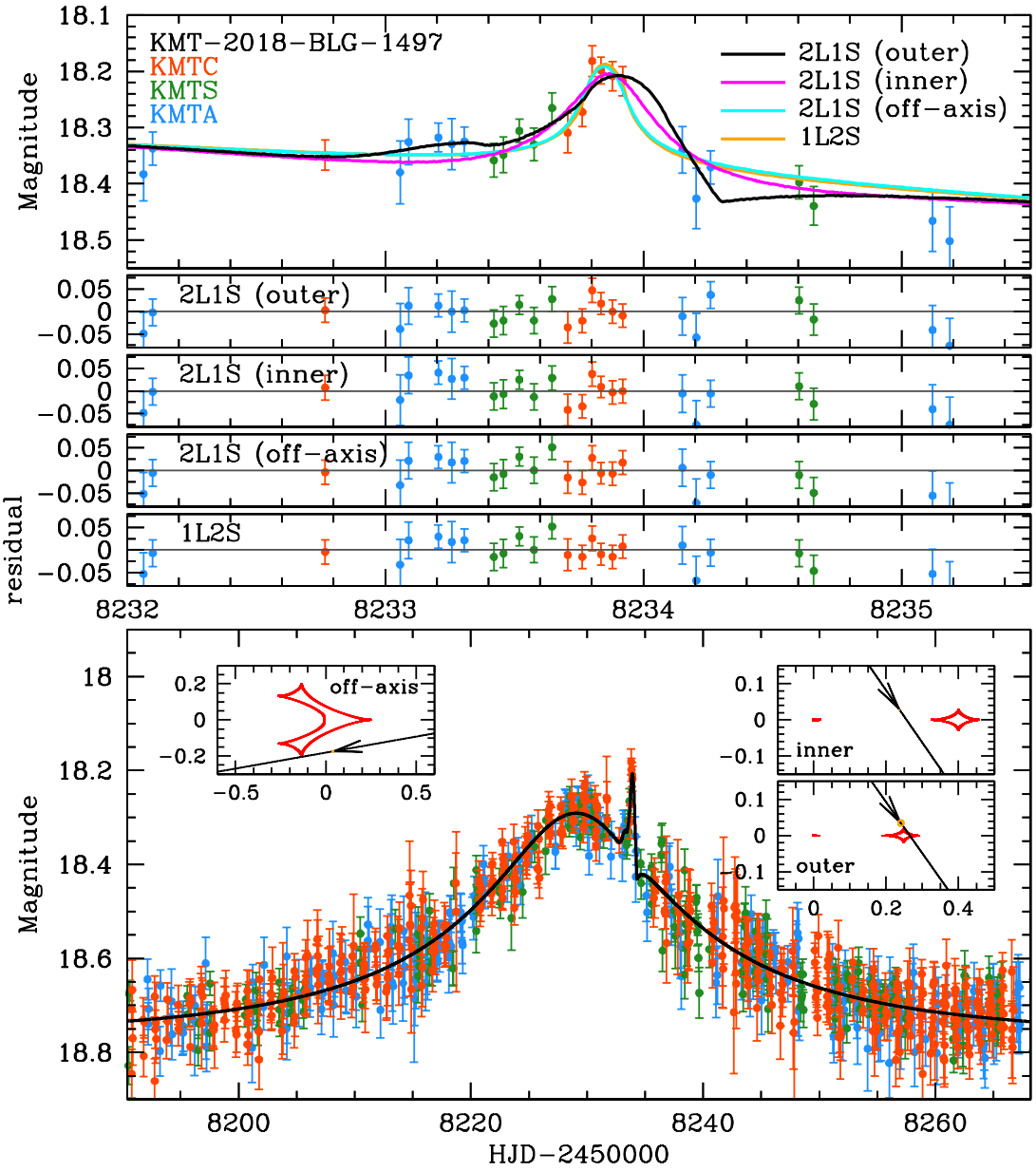


Fig. 8.— Data (color-coded by observatory) together with the predictions and residuals for the models of KMT-2018-BLG-1497 specified in Table 9. The short "bump" at $t_{\rm anom} = 8233.9$ has 4 possible explanations: 2 from an "inner/outer" degeneracy (right insets), one from an off-axis cusp approach (left inset) [together with $-3.7 \lesssim \log q \lesssim -1.8$], or 1L2S model. The last has $\Delta\chi^2 = 2.1$, and there are no other arguments against it. Therefore, this event should not be cataloged as planetary.

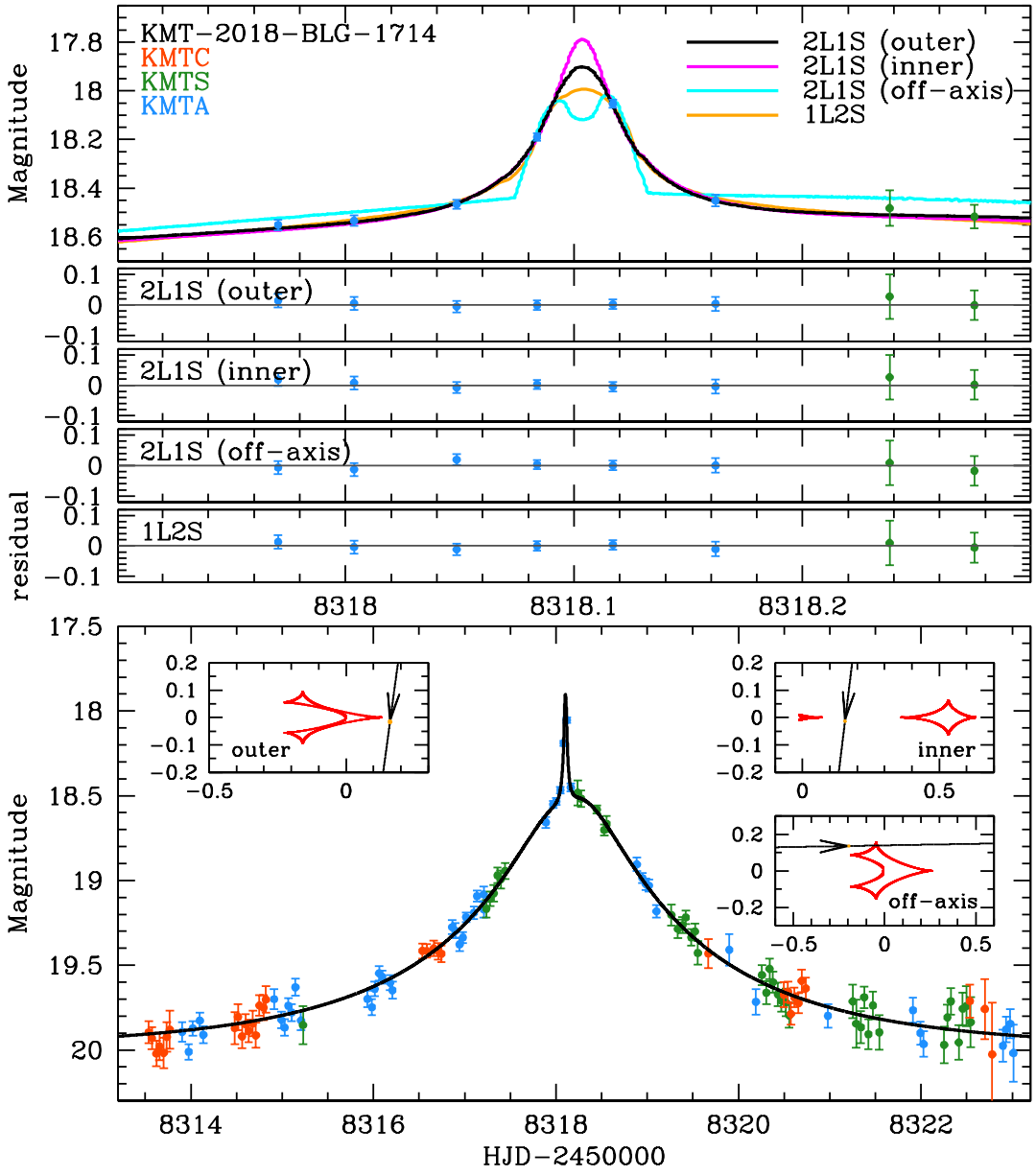


Fig. 9.— Data (color-coded by observatory) together with the predictions and residuals for the models of KMT-2018-BLG-1714 specified in Table 10. The short "bump" at $t_{\rm anom} = 8318.10$ has 4 possible explanations: 2 from an "inner/outer" degeneracy (top insets), one from an off-axis cusp approach (lower right inset) [together with $-2.4 \lesssim \log q \lesssim -1.8$], or 1L2S model. The last has $\Delta\chi^2 = 0.9$, and there are no other arguments against it. Therefore, this event should not be cataloged as planetary.

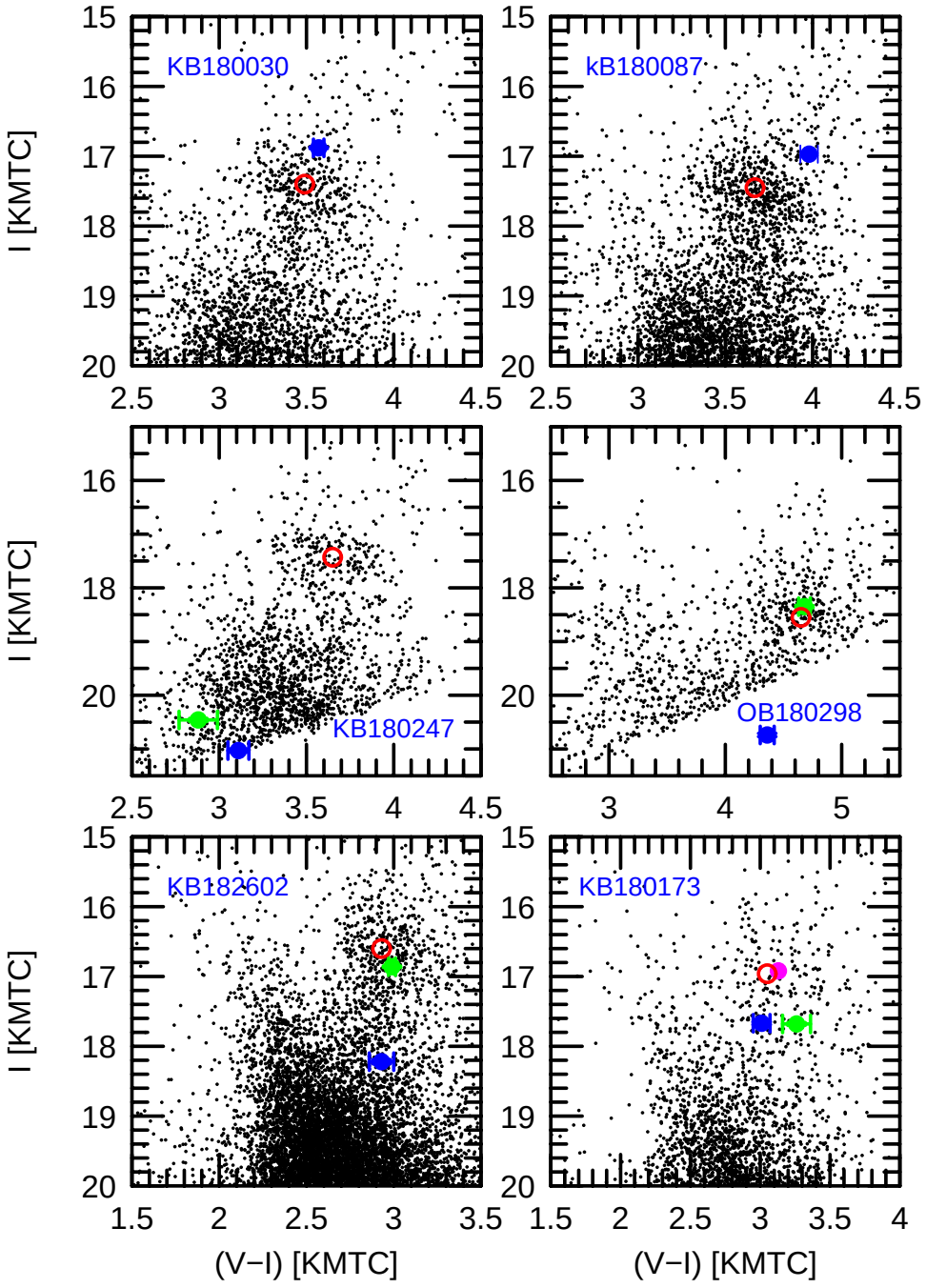


Fig. 10.— Color-magnitude diagrams for 6 of the events analyzed in this paper, each identified by an abbreviation, e.g., KB180030 for KMT-2018-BLG-0030. The centroid of the red clump and the lens position are always shown in red and blue, respectively. Where relevant, the blended light is shown in green. In one case (KB180173), we show the baseline object in magenta. When there are multiple solutions, we show only the source and blend for the lowest-χ^2 solution.

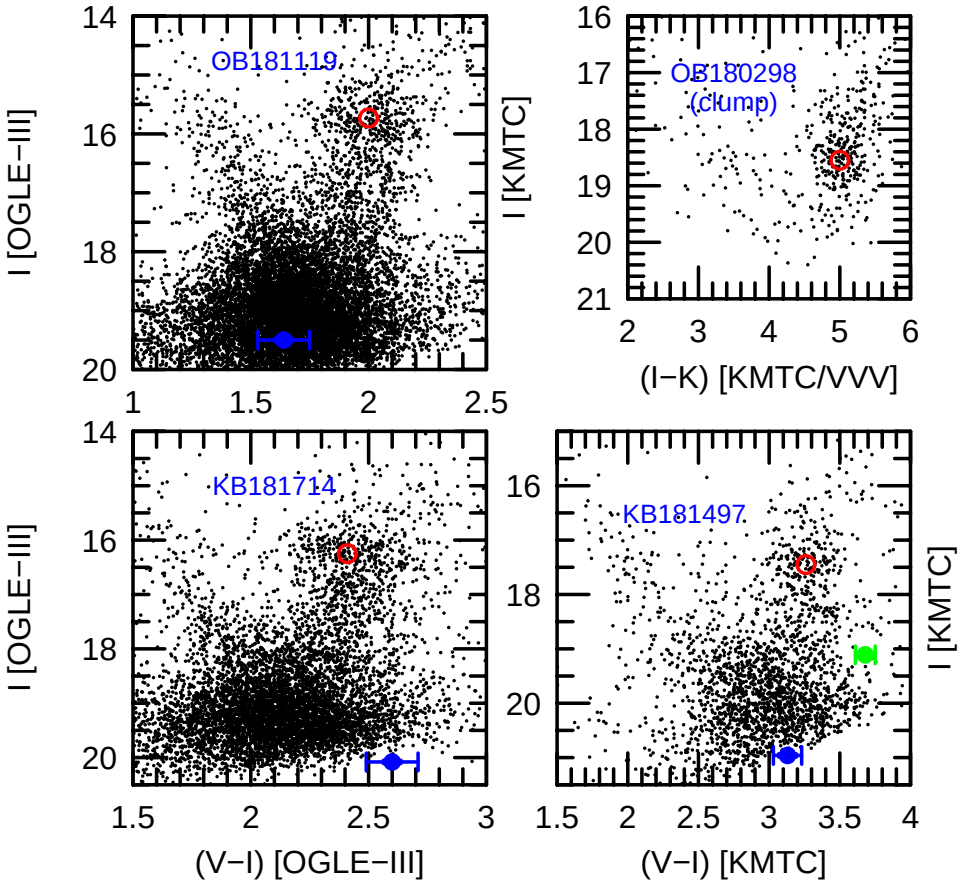


Fig. 11.— Same as Figure 10, but for the remaining 3 events (normal-sized panels). The undersized panel shows the determination of $I_{\rm cl}$ from an $[(I-K), I]$ CMD. See Section 4.4.

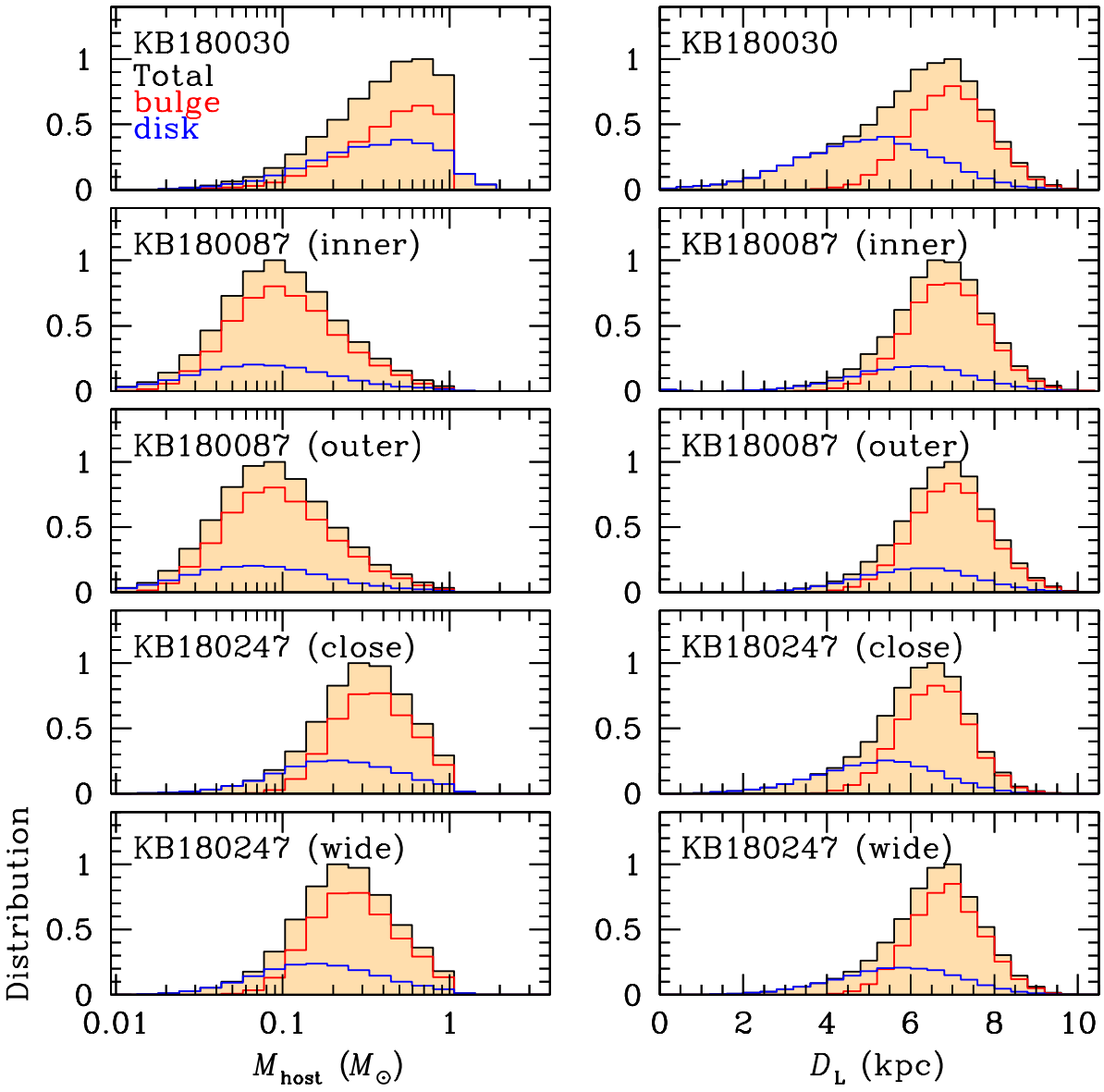


Fig. 12.— Histograms of the host mass (left) and lens distance (right) for 3 of the 6 unambiguously planetary events, as derived from the Bayesian analysis. Disk (blue) and bulge (red) distributions are shown separately, with their total shown in black.

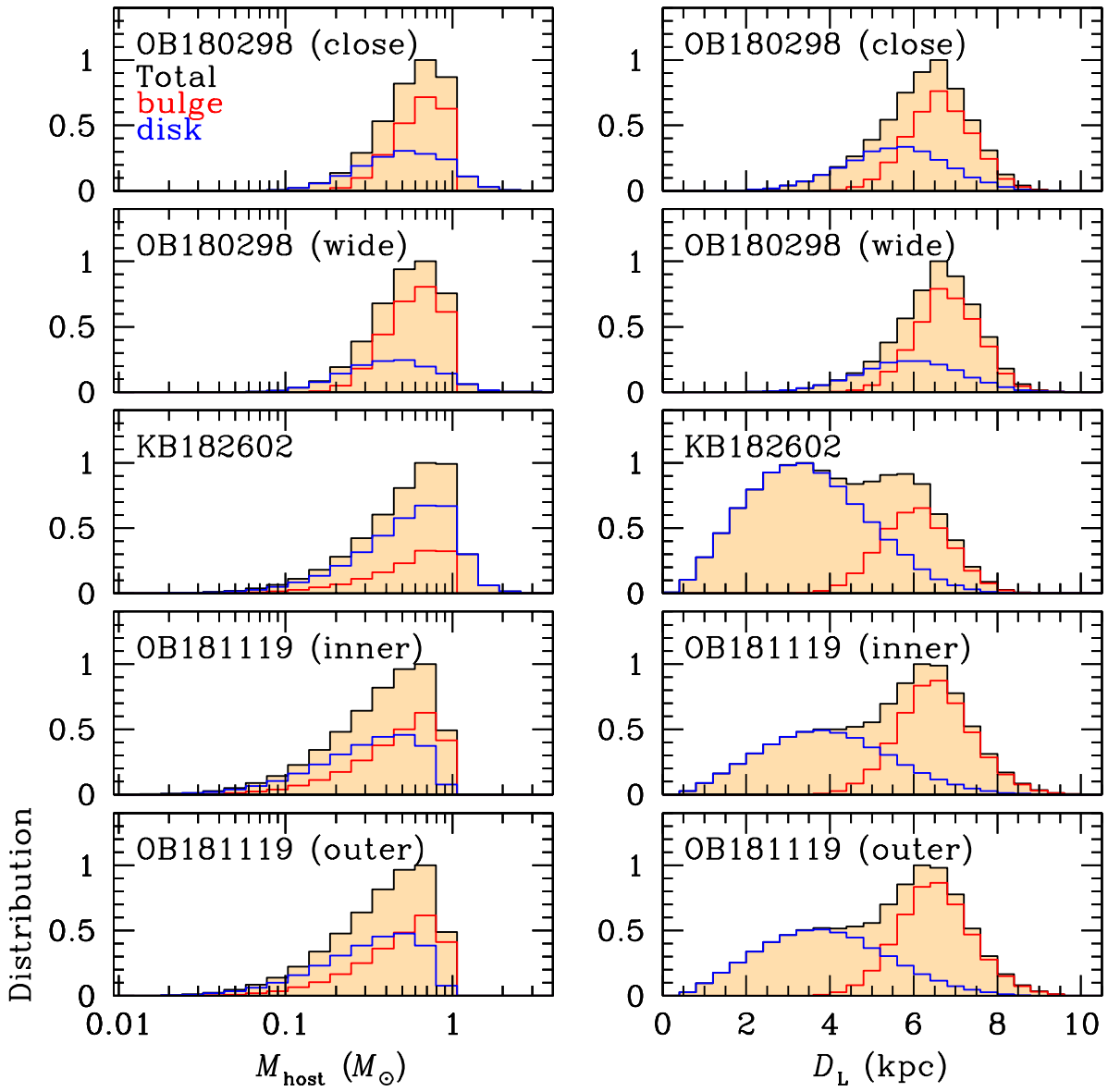


Fig. 13.— Same as Figure 12, except that this figure shows the remaining 3 unambiguously planetary events.

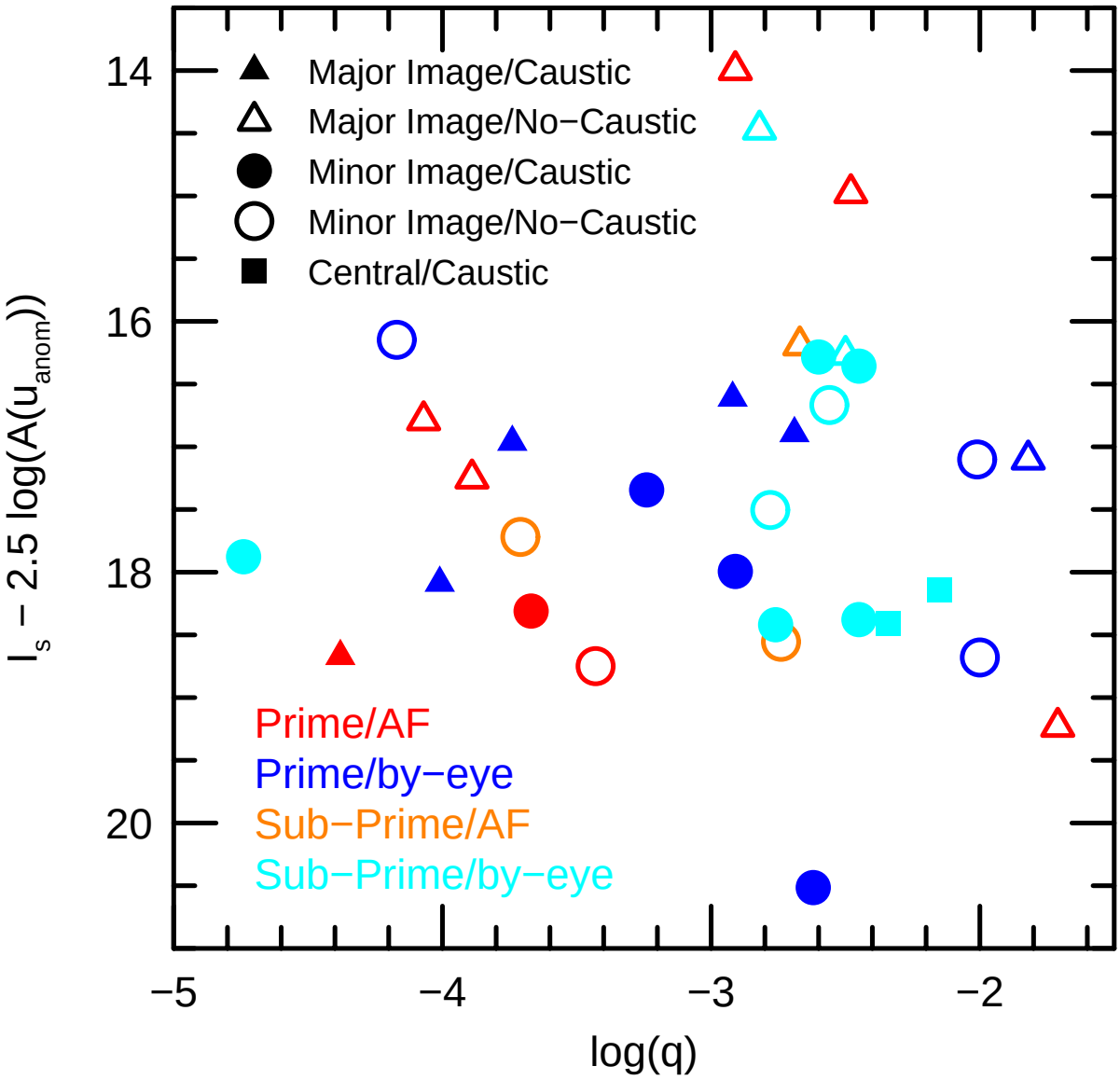


Fig. 14.— 6-dimensional scatter plot of 33 planetary events. (1) Abscissa: log mass ratio. (2) Ordinate: source magnitude of unperturbed event at time of anomaly. (3) Primary (red, blue) vs. non-primary (orange, cyan) colors: prime vs. sub-prime fields. (4) Reddish (red, orange) vs. bluish (blue, cyan) colors: AnomalyFinder vs. by-eye discoveries. (5) Filled vs. open symbols: caustic-crossing vs. non-caustic-crossing anomalies. (6) Shape: Major-image (triangles), minor-image (circles), and central-caustic (squares) perturbations. The two most important patterns are: (A) a threshold of detections at $I_S - 2.5 \log[A(u_{\rm anom})] = 18.75$ and (B) the dearth of by-eye discoveries of non-caustic-crossing anomalies (bluish open symbols) for $\log q < -3$.